Feedback control of flow-induced vibration of a sphere

T. McQueen[1,†], J. Zhao[1], J. Sheridan[1] and M. C. Thompson[1]

[1]Fluids Laboratory for Aeronautical and Industrial Research (FLAIR),
Department of Mechanical and Aerospace Engineering, Monash University,
Melbourne, VIC 3800, Australia

The flow-induced vibration of a sphere elastically mounted in the cross-flow direction with imposed feedback rotation was investigated experimentally. The application of rotation provides a means to exercise control over the vibration response of axisymmetric three-dimensional objects. Both the rotational amplitude, which was imposed in proportion to sphere transverse displacement, and the phase of the control signal were varied over a broad parameter space comprising: a non-dimensionalised proportional gain ($0.5 \leqslant K_p^* \leqslant 2$); rotation phase ($0° \leqslant \phi_{rot} \leqslant 360°$), which is the phase between the applied sphere rotation and the transverse displacement; and reduced velocity ($3 \leqslant U^* \leqslant 20$). The corresponding Reynolds number range was ($3900 \lesssim Re \lesssim 25\,800$). The structural vibration, fluid forces and wake structure were examined to characterise the effect of the imposed rotation. It was found that the rotation not only altered the magnitude of the vibration response, either amplifying or attenuating the response depending on operating conditions, but it also altered the reduced velocity at which vibrations commenced, the vibration frequency and periodicity and significantly altered the phase between the transverse fluid force and displacement. It was possible to almost completely suppress the vibration in the mode I, mode II and mode III transition regimes for imposed rotation over the ranges $90° \lesssim \phi_{rot} \lesssim 180°$, $15° \lesssim \phi_{rot} \lesssim 135°$ and $0° \lesssim \phi_{rot} \lesssim 120°$, respectively. In particular, this could be achieved at effective rotation rates well below those required by using open-loop control (Sareen *et al.*, *J. Fluid Mech.*, vol. 837, 2018, pp. 258–292). Past the peak of mode II, a 'galloping-like' response, similar to that reported by Vicente-Ludlam *et al.* (*J. Fluid Mech.*, vol. 847, 2018, pp. 93–118) for the circular cylinder, was observed with an increase in vibration amplitude of up to 368 % at the highest reduced velocity tested ($U^* = 20$). Particle image velocimetry measurements revealed a change in the timing and spatial position of the streamwise vortex structures with imposed rotation. Contrary to what has been observed for the circular cylinder, however, no de-synchronisation between vortex shedding and sphere motion was observed.

Key words: flow–structure interactions, wakes

† Email address for correspondence: thomas.mcqueen@monash.edu

1. Introduction

Flow-induced vibration (FIV) is observed in a diverse range of engineering applications. Traditionally, the primary concern for engineers has been the effect of vibration on the structural integrity of objects. In particular, the potential for a diminished usable life or critical failure of a structure poses a significant threat to safety and may result in detrimental economic effects. This practical concern, along with an interest in the fundamental fluid mechanics, has resulted in a broad literature base that reveals, in detail, the physical mechanisms behind FIV. Predominantly, the focus of past research has been the canonical case of the vibration response of a circular cylinder. Reviews by Bearman (1984), Sarpkaya (2004) and Williamson & Govardhan (2004) and books by Blevins (1990), Païdoussis, Price & de Langre (2010) and Naudascher & Rockwell (2012) describe how a resonance between the system response and the fluid forces results in the vibration of an object. Naudascher & Rockwell (2012) defined three sources of excitation leading to vibration. Namely, extraneously induced excitation, instability-induced excitation and movement-induced excitation, the latter two of which are intrinsically linked to the fluid–structure system and are of interest to this investigation. Instability-induced excitations are most often a result of periodic vortex shedding from a structure. This is referred to as vortex-induced vibration (VIV). Movement-induced excitation, as the name suggests, arises due to movement of a structure. This movement may arise due to an initial disturbance, which in turn results in self-sustained motion due to an alteration of the fluid force on the structure over a vibration cycle (e.g. galloping). The comprehensive knowledge base that researchers have developed on these forms of FIV has allowed engineers to mitigate or even eliminate the vibration of many structures.

More recently, researchers have also begun to investigate the potential to use FIV as a method to extract energy from a flow. The predominant benefits often reported are that energy can be extracted at flow speeds below those at which traditional fluid energy harvesting devices, such as turbines, are efficient, and that the geometry of FIV energy harvesting devices may make them more suitable to certain locations such as rivers. The most well-developed energy generation device that harvests the power of VIV is the vortex-induced vibration for aquatic clean energy (VIVACE) generator outlined by Bernitsas *et al.* (2008). This device harnesses the power of VIV using multiple circular cylinders constrained to one degree of freedom. Devices harnessing the power of other FIV phenomena including flutter (Michelin & Doaré 2013) and galloping (Hémon, Amandolese & Andrianne 2017) are also being researched as potential candidates for efficient energy generation.

Although to a lesser extent than for the circular cylinder, the sphere geometry has also been investigated to determine the physical mechanisms causing VIV of three-dimensional geometries. The first to investigate the vibration response of a sphere systematically were Govardhan & Williamson (1997) and Williamson & Govardhan (1997). Prior to their investigations, it was unclear whether a tethered sphere would substantially vibrate, given that the alternating vortex shedding driving VIV of a circular cylinder does not occur in the sphere wake. They found that a tethered sphere would indeed vibrate and that it would do so at amplitudes of up to approximately one sphere diameter over a broad range of flow speeds. In a similar manner to the work undertaken for a circular cylinder, Jauvtis, Govardhan & Williamson (2001) described a series of vibration modes that could be observed for a sphere. Mode I and mode II were defined as the regimes where resonance was observed. The resonance occurs where the equivalent fixed-body vortex shedding frequency remains close to the natural frequency of the oscillating system. For a sphere, a significant change in timing of the fluid forcing occurs over the transition

between the mode I and mode II regimes. Jauvtis *et al.* (2001) also identified mode III and mode IV regimes that occurred over reduced velocity ranges of $20 \lesssim U^* \lesssim 40$ and $U^* \gtrsim 100$, respectively, at least for high mass-ratio spheres. Lastly, they observed that, at these higher reduced velocities, the primary vortex structures form at a much higher frequency than the body oscillation frequency. In addition to the tethered sphere, Govardhan & Williamson (2005) examined a sphere constrained to one degree of freedom, free to oscillate transverse to the free-stream flow. They found a similar amplitude response to the tethered case; the main difference being a continuation of vibration in the transition from mode II to mode III regimes. Using particle image velocimetry (PIV), Govardhan & Williamson (2005) were able to visualise the formation of vortex loops in the wake of the vibrating sphere, likening the generation of transverse lift, leading to vibration, to that of the lift generation associated with aircraft wing-tip trailing vortices. Recently, numerical simulations have shown that the resonant modes also occur at much lower Reynolds numbers ($Re \sim 1000$), although at very low Reynolds numbers ($Re \sim 300$) only mode I appears (e.g. Behara, Borazjani & Sotiropoulos 2011; Behara & Sotiropoulos 2016; Rajamuni, Thompson & Hourigan 2018*a,b*). More recently, Eshbal *et al.* (2019) conducted tomographic PIV measurements in the wake of a tethered sphere. They reported the formation of 'omega-shaped' vortices, the legs of which merged as the vortex structure convected downstream, transforming into a vortex ring as observed in dye visualisations by Govardhan & Williamson (2005). They also identified a weak vortex filament that connected the vortex ring to upstream vortex structures.

Given the implications of structural failure, or conversely the potential to harvest energy from VIV, there is a clear motivation to manipulate the vibration response of an object to our advantage. Several studies have investigated the potential for passive control methods to suppress vibration. Helical strakes (Zhou *et al.* 2011), control rods (Wu *et al.* 2012) and spanwise grooves (Law & Jaiman 2018) are examples of methods that have been employed for the circular cylinder. Active control methods have also been examined, examples include moving surface boundary-layer control (Korkischko & Meneghini 2012), wake control cylinders (Silva-Ortega & Assi 2017), suction and blowing (Wang *et al.* 2016) and body rotation (Wong *et al.* 2017, 2018; Zhao *et al.* 2018). van Hout, Katz & Greenblatt (2013*a*) appear to be the first to attempt to control the vibration response of a sphere. Using acoustic control, in the form of speakers mounted to wind-tunnel walls, they imposed acoustic excitation at approximately the shear-layer instability frequency, which amplified vibrations in the mode III regime. Perturbing the flow at higher frequencies, they were able to almost completely suppress vibrations in the mode I and mode II regimes. More recently, Sareen *et al.* (2018*a,b*) implemented imposed rotation using a sphere constrained to one degree of freedom. They found it more difficult to suppress vibration in the mode I regime, where the vortex shedding frequency is close to the natural frequency of the system. Implementing rotary oscillations, Sareen *et al.* (2018*b*) were able to force body vibration to 'lock-on' to the imposed forcing frequency when the forcing frequency was close to natural frequency of the system. In this 'lock-on' regime, close to, but not at the natural frequency of the system, the vibrations were greatly attenuated.

Whilst effective, the open-loop control strategies implemented by Sareen *et al.* (2018*a,b*) have no direct coupling to the system dynamics. Rather, they relied on the vortex dynamics naturally locking to the imposed forcing frequency. For a circular cylinder, Vicente-Ludlam, Barrero-Gil & Velazquez (2018) were able to link imposed forcing to the system dynamics by rotating the cylinder in proportion to either its transverse position or velocity. By using feedback in proportion to displacement they

were able to gain greater control over the vibration response for much of the reduced velocity range examined. They were able to either amplify or attenuate the vibration response by setting the proportional gain to rotate the leading side of the cylinder with (negative) or against (positive) the direction of the free-stream flow. For large negative gain values they observed a 'galloping-like' response and postulated that the large-amplitude vibration was due to rotation-induced forces as opposed to being driven by vortex shedding, as seen for the natural response. This was supported by the observation that for the 'galloping-like' response, the frequency of vibration remained close to the natural frequency of the system, whilst vortices were shed independently at approximately the Strouhal number observed for an equivalent stationary cylinder. Using a quasi-steady analysis, they estimated the minimum proportional gain value required for a 'galloping-like' response, and showed that this response is not possible for rotation in proportion to cylinder velocity.

Sareen *et al.* (2018*a*,*b*) demonstrated the potential to alter the vibration response of three-dimensional structures by implementing open-loop control in the form of imposed rotation of a sphere. For a two-dimensional cylinder, Vicente-Ludlam *et al.* (2018) demonstrated that linking the instantaneous rotation to the system dynamics enabled a greater degree of control over the vibration response. Therefore, the first question to be addressed in this paper is: to what extent does linking the imposed rotation to the system dynamics of a sphere enable control of the vibration response? Vicente-Ludlam *et al.* (2018) implemented feedback control with positive and negative gain terms in proportion to both cylinder displacement and velocity separately. The imposed rotation can be related to the phase angle between applied body rotation and transverse body displacement, which is referred to as the rotation phase (ϕ_{rot}). For Vicente-Ludlam *et al.* (2018), this resulted in imposed rotation at four distinct values: $\phi_{rot} = 0°$, $90°$, $180°$ and $270°$. From their study, it is evident that altering the rotation phase can significantly alter the vibration response. From a practical perspective, unlike the proportional gain term, altering the rotation phase does not alter the required energy input. Therefore, optimising the rotation phase offers an opportunity to enhance either vibration suppression or amplification without increasing energy input to the system. As such, the second focus of this study is to conduct a systematic investigation to determine the effect of varying the rotation phase on the vibration response of a sphere.

The structure of the paper is as follows. In §2 the experimental method and rotation control laws are detailed, followed by a validation of the experimental set-up in §2.3. In §3 the vibration response of a sphere with imposed rotation in proportion to transverse displacement is presented. This is followed by a discussion on the effect varying phase has on the vibration response. Finally, in §4 the outcomes of the study are summarised and concluding remarks presented.

Throughout this paper, the effects of imposed rotation are often compared to the standard vibration response with no imposed rotation. Hereafter, the response of the sphere with no imposed rotation will be referred to as the 'natural' response.

2. Experimental methodology

2.1. *System modelling and control laws*

The system studied here consists of an elastically mounted sphere that is free to oscillate only in the direction transverse to the free-stream flow. Rotation (for control) of the sphere is imposed about the axis perpendicular to the direction of free-stream flow and the free-vibration axis. Figure 1 illustrates the fluid–structure interaction set-up looking down along the rotation axis.
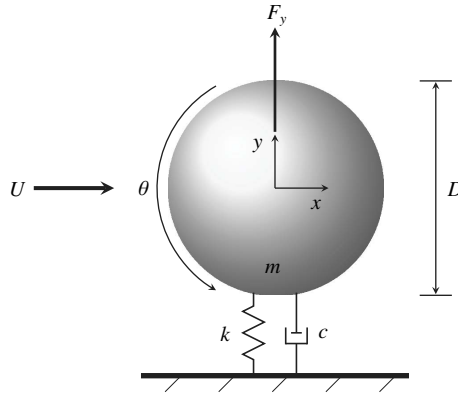
FIGURE 1. Schematic of the experimental set-up highlighting the key parameters for the transverse VIV of a rotating sphere. The hydro-elastic system is simplified as a one-degree-of-freedom system constrained to move in the cross-flow direction. The axis of rotation is perpendicular to both the free-stream flow direction (x-axis) and the oscillation axis (y-axis). Here, U is the free-stream velocity, F_y is the transverse force, k is the spring constant, D is the sphere diameter, m is the oscillating mass, c is the structural damping and θ is the angular position of the sphere.

The governing equation of motion for transverse vibration can be expressed as

$$m\ddot{y} + c\dot{y} + ky = F_y, \tag{2.1}$$

where y is the displacement in the transverse direction, m is the oscillating mass of the system, c is the structural damping, k is the structural stiffness and F_y is the transverse force. Table 1 shows the relevant non-dimensional parameters for the study.

In this investigation, active control of cross-stream vibration was instigated through controlled sphere rotation. In particular, the sphere was rotated in proportion to its transverse displacement, y. Firstly, the rotation was imposed according to

$$\theta_s = K_p y, \tag{2.2}$$

where θ_s is the angular displacement of the sphere and K_p is the proportional gain. Next, this control law was modified to allow a phase difference between the instantaneous transverse displacement and the applied rotational displacement. To construct this law, the Hilbert transform, $H(y)$, of the displacement signal is first evaluated in real time. The purpose of the Hilbert transform is to impart a $-\pi/2$ phase shift to the transverse displacement signal, i.e. $y(\phi - \pi/2) = H(y(\phi))$. This provides a means of constructing a control signal with any desired phase shift,

$$\theta_s = K_p[\cos(\phi_d)y + \sin(\phi_d)(-H(y))], \tag{2.3}$$

where ϕ_d is the required phase shift in radians, and $H(y)$ is the Hilbert transform of the transverse displacement signal, y. To implement this law in a real-time control system, a Hilbert transform filter was designed in Simulink®. Furthermore, using the same notation as Vicente-Ludlam *et al.* (2018), the diameter of the sphere, D, is introduced as a reference length so that the rotation law can be made dimensionless. Thus, the two dimensionless rotation laws implemented are

$$\theta_s = K_p^* y^* \tag{2.4}$$

Amplitude ratio	A^*	$\sqrt{2}A_{rms}/D$
Damping ratio	ζ	$c/\sqrt{k(m+m_A)}$
Frequency ratio	f^*	f/f_n
Mass ratio	m^*	m/m_d
Mass-damping parameter	ξ	$(m^*+C_A)\zeta$
Reduced velocity	U^*	U/f_nD
Reynolds number	Re	$\rho UD/\mu$
Scaled normalised velocity	U_s^*	$(U^*/f^*)S=f_{vo}/f$
Strouhal number	S	$f_{vo}D/U$
Transverse force coefficient	C_y	$F_y/(\frac{1}{8}\rho U^2\pi D^2)$
Transverse force frequency ratio	$f_{C_y}^*$	f_{C_y}/f_n

TABLE 1. Relevant non-dimensional parameters. Here, A^* is the root-mean-square value of the vibration amplitude in the y direction, D is the sphere diameter, c is the structural damping, k is the structural stiffness, m is the oscillating mass, $m_A = C_A m_d$ is the added mass, m_d is the displaced mass of the fluid, C_A is the added mass coefficient (0.5 for a sphere), f_n is the natural frequency of the system in quiescent water, f_{vo} is the equivalent fixed-body vortex shedding frequency, f is the body oscillating frequency and F_y is the transverse fluid force acting on the sphere.

and

$$\theta_s = K_p^*[\cos(\phi_d)y^* + \sin(\phi_d)(-H(y^*))], \tag{2.5}$$

where $y^* = y/D$ is the non-dimensional transverse displacement and $K_p^* = K_pD$ is the normalised proportional gain. As an example, if $K_p^* = 1$, $\phi_d = 0$, and the sphere was displaced one diameter in the positive y direction, the leading side of the sphere would be rotated one radian towards the oncoming free-stream flow.

2.2. *Experimental set-up*

The investigation was conducted in the recirculating free-surface water channel of the Fluids Laboratory for Aeronautical and Industrial Research (FLAIR) at Monash University. The water channel has a working section of 600 mm in width, 800 mm in depth and 4000 mm in length. The free-stream turbulence level is less than 1 % over the flow-rate range investigated. During experiments, the free-stream velocity was varied within the range $55 \leqslant U \leqslant 370$ mm s^{-1}. The sphere, which was subject to VIV oscillatory forcing, was elastically mounted using a low-friction air-bearing system situated above the water channel. The system provides low structural damping. The structural stiffness was adjustable by modifying the type, quantity and position of stainless-steel springs. A schematic of the experimental set-up is shown in figure 2. For more details on the air-bearing system and its characterisation, refer to Nemes *et al.* (2012) and Zhao *et al.* (2014). The 70 mm diameter sphere, CNC machined from medium density precision modelling board (RenShape 460), was mounted by a 3 mm hardened stainless-steel rod to a servo motor (Maxon Motor, EC-max 4-pole 22, equipped with a rotary encoder with a resolution of 5000 counts per revolution). To minimise deflection of the rod with the imposed rotary oscillations, a 6.35 mm stationary cylindrical shroud with a stainless-steel bearing and nylon bushing supported part of its length. This provided stiffness to the mounting rod and limited (Magnus) forcing that would be induced if the shroud rotated. The immersed
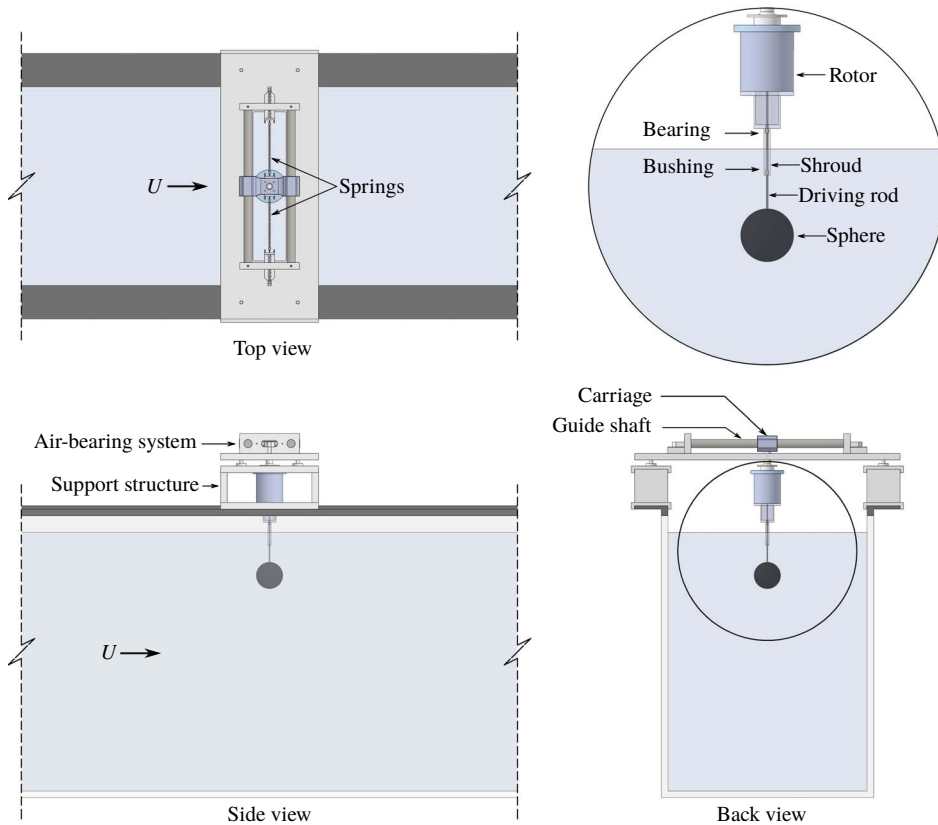
FIGURE 2. Schematic of the experimental set-up for the current study.

length of the sphere was $1D$ as recommended by Govardhan & Williamson (2005) and Sareen *et al.* (2018*c*). The shroud extended $0.3D$ below the free surface. The diameter ratio between the (un-shrouded) rod and sphere was 23.3. Evidently, the presence of the mounting rod will have some effect on the flow in proximity to the sphere. As a necessity of the experimental set-up, a compromise between the need to rigidly mount the sphere and minimise the influence of the mounting rod was made. Sareen *et al.* (2018*a*) verified that the presence of a mounting rod (of the same diameter ratio as used in this investigation) did not appreciably influence the amplitude of the vibration. However, there may still be noticeable differences to the wake structure. The Reynolds number range investigated is $165 \lesssim Re \lesssim 1100$ for the un-shrouded rod and $350 \lesssim Re \lesssim 2340$ for the shrouded rod. Vortex shedding will therefore occur for all reduced velocities investigated (Williamson 1996). van Hout *et al.* (2018) performed detailed tomographic PIV measurements of a sphere with a mounting rod (diameter ratio 6) immersed in a turbulent boundary layer. Whilst they observed clear vortex shedding from the rod in proximity to the sphere, they noted that the there was at least an order of magnitude less energy in the wake of the rod in comparison to the sphere and that no distinct frequency peak associated with the rod was observable in the sphere wake. Additionally, for a stationary sphere with no mounting rod, vortex shedding occurs at random azimuths. However, when a mounting rod is introduced, axisymmetry is broken and vortex shedding is more

likely to occur at certain azimuths (Grandemange, Gohlke & Cadot 2014). Whilst it is noted that the presence of the rod may affect the wake structures, this effect is expected to be negligible in the context of this investigation.

The transverse displacement of the sphere was measured using a digital linear encoder with a resolution of 1 µm (model RGH24; Renishaw, UK). As a result of the highly accurate digital displacement measurements, it is possible to derive the sphere velocity and acceleration with good accuracy. In turn, the lift force and phase between lift and displacement can be determined. Zhao *et al.* (2018) and Sareen *et al.* (2018*a*) have verified this methodology for the circular cylinder and sphere, respectively, using the same air-bearing system and comparisons to independent measurements of lift force obtained using a force balance. The mass ratio was $m^* = 10.1$. Free decay tests were conducted to determine the natural frequency and structural damping ratio of the system in air and water. The natural frequency was $f_{na} = 0.270$ Hz in air and $f_n = 0.265$ Hz in water. The structural damping ratio with consideration of the added mass (see Govardhan & Williamson 2005) was found to be $\zeta = 4.24 \times 10^{-3}$.

The rotation was implemented using Beckhoff Automation GmbH hardware and Beckhoff TwinCAT® 3 software. The system consisted of a coupler (model EK1100), analogue input (model EL2124), digital input (model EL3124), encoder module (model EL5001) and motor controller (model MAXPOS 50/5, Maxon Group). The sampling rate of the system was 2 kHz. For imposed rotation implemented using (2.4), the maximum observed phase lag between transverse displacement and desired rotation angle was 1.5°. For imposed rotation implemented using (2.5), a finite impulse response filter was designed using the Simulink® 'Hilbert Filter' block. Due to the implementation of the filter and further filtering required to smooth the output signal, an increase in maximum phase lag of up to approximately 8° was observed in the worst case. The desired rotation phase, was adjusted prior to testing to account for this delay in an approximate manner. However, all values of rotation phase presented in this study were calculated during post-processing, thus the actual rotation phase, may differ from the theoretical phase shift, ϕ_d, given in equation 2.5. The Hilbert filter also slightly affected the amplitude of the output signal, causing the sphere position to deviate from the desired value. A mean variation of 1.96 % and standard deviation of 2.40 % were observed. Whilst the phase-shifted control law (2.5) is able to accurately impose a specified phase shift, with small-amplitude less-periodic vibrations, larger variations in the imposed rotation amplitude are seen. Excluding data points where $y/D < 0.1$, the mean variation and standard deviation of the vibration amplitude are reduced to 1.23 % and 1.25 %, respectively. Although less than optimal, this level of accuracy was deemed suitable to show the trend of the vibration response to phase variation. Perhaps unsurprisingly, where the signal became highly non-periodic, for very small vibration amplitudes, the phase of the displacement signal became unclear and it became difficult for the second control law to determine the required sphere rotation.

To gain an insight into the wake dynamics, PIV was employed in the equatorial (x–y) and the cross-stream (y–z) planes at $x/D = 1.5$. The flow was seeded using hollow micro-spheres (model Sphericel 110P8; Potters Industries Inc.) with normal diameter 13 µm and specific weight 1.1 g cm^{-3}. A high-speed camera (Dimax S4, PCO AG, Germany) with resolution 2016×2016 pixel^2 and a 105 mm lens (Nikkon, Japan) was used in conjunction with a 5 W continuous laser (MLL-N-532 mm, CNI, China) that produced a 3 mm thick laser sheet to capture the images. For the y–z plane, a mirror was placed approximately 10D downstream of the sphere at 45°

to the free-stream flow. To capture large-amplitude oscillations in the y–z plane, a field of view capturing only half the oscillation cycle was used. For the x–y, y–z, and reduced field of view y–z planes respectively, the magnification factors were 6.62 pixel mm^{-1}, 9.6 pixel mm^{-1} and 10.2 pixel mm^{-1}. In-house cross-correlation software, originally developed by Fouras, Lo Jacono & Hourigan (2008), was used to correlate interrogation windows of size 32×32 pixel^2 with an overlap of 50 % to obtain the velocity fields. This corresponded to a velocity vector field of 125×125 vectors for the x–y plane, and 125×87 vectors for the y–z plane. Two sets of data, comprising totals of 6200 image pairs for the x–y plane, and 8800 image pairs for the y–z plane, were acquired at 10 Hz. Subsequently, the two out-of-plane components of the vorticity field were calculated. The vector fields were phase averaged by sorting them into 48 bins based on the sphere displacement. Each bin consisted of at least 120 vector fields. Finally, the phase-averaged vorticity fields were smoothed slightly using Gaussian smoothing to remove short length scale structures highlighting the larger-scale structures, which are of interest to this study.

2.3. *Validation*

The experimental set-up was first validated by comparing results obtained without imposed rotation to those of Govardhan & Williamson (2005) and Sareen *et al.* (2018*a*). Sareen *et al.* (2018*a*), investigating imposed constant rotation on a sphere, previously validated the experimental facility and as such only a brief (re-)validation is presented here. Figure 3 compares the amplitude response of the sphere against scaled normalised velocity (U_s^*) for the three studies. The amplitude response has been plotted against $U_s^* = (U^*/f^*)S$ to allow direct comparison to the previous studies. Govardhan & Williamson (2005) demonstrated that plotting the amplitude response against U_s^* collapses data sets with varying mass-damping parameters well. Two data sets from Govardhan & Williamson (2005) are used for comparison here: $m^* = 7$ with mass damping $(m^* + C_A)\zeta = 0.03$; and $m^* = 53.7$ with mass damping $(m^* + C_A)\zeta = 0.92$. The data set from Sareen *et al.* (2018*a*) has values of $m^* = 14.2$ with mass damping $(m^* + C_A)\zeta = 0.021$.

Good agreement can be seen between the instigation of the vibration response at $U_s^* \approx 0.87$ and the subsequent trend of the response through mode I, mode II and mode III transition regimes. For a sphere elastically constrained to one degree of freedom, over the range of mass-damping parameters examined in figure 3, there is no sharp distinction between the first two modes of vibration (although a slight inflection is visible in the response curve at $U_s^* \simeq 1.25$). Rather, a slow change in vortex phase from approximately 40° to 160° distinguishes modes I and II (Govardhan & Williamson 2005). The peak amplitude response is observed in the mode II regime, where the phase between transverse displacement and the fluid force acting on the body, termed total phase (ϕ_{total}), rises to 90°. Past the peak of mode II, there is a transition region where the response becomes less periodic and the amplitude plateaus. As discussed by Govardhan & Williamson (2005) and Sareen *et al.* (2018*a*), the differences in the amplitude response between studies may be attributed to the difference in experimental conditions; primarily the difference in mass ratio and structural damping.

3. Results

To determine the effect of sphere rotation in proportion to transverse displacement, the two control laws detailed in § 2.1 were implemented. Firstly, as per equation (2.4),
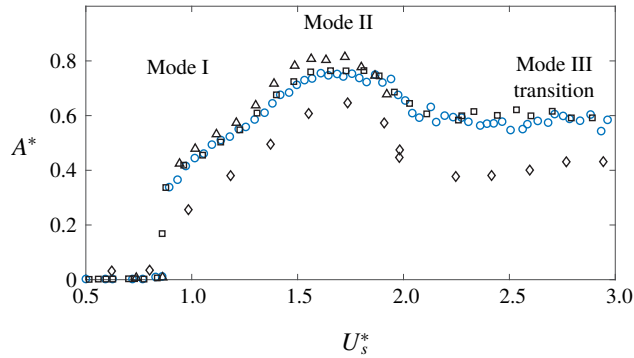
FIGURE 3. Comparison of the vibration response for a non-rotating sphere undergoing VIV. The blue circles (○) show the results from the current study with $(m^* + C_A)\zeta = 0.045$; the triangles (△) show the results from Govardhan & Williamson (2005) with $(m^* + C_A)\zeta = 0.03$; the diamonds (◇) show the results from Govardhan & Williamson (2005) with $(m^* + C_A)\zeta = 0.92$ (with $m^* = 53.7$); the squares (□) show the results from Sareen *et al.* (2018*a*) with $(m^* + C_A)\zeta = 0.021$.

rotation was imposed with both the leading side (in the transverse direction) of the sphere moving against ($\phi_{rot} = 0°$) and with ($\phi_{rot} = 180°$) the oncoming free-stream flow, over the range $3 \leqslant U^* \leqslant 20$. Secondly, to determine the effect of varying ϕ_{rot}, rotation was implemented according to (2.5) over the range $0° \leqslant \phi_{rot} \leqslant 360°$ in the mode I ($U^* = 6$), mode II ($U^* = 10$) and mode III transition ($U^* = 14$) regimes. For both rotation laws, proportional gain values of $K_p^* = 0.5, 1, 2,$ and 4 were investigated.

3.1. *Control imposed with a rotation phase of* $0°$

To develop an understanding of the potential effect of imposed rotation on the vibration response of a sphere, it is worthwhile to first consider the isolated contribution of the Magnus effect induced by the imposed rotation over a vibration cycle. Put succinctly, the Magnus effect results in a lift force perpendicular to the axis of rotation, in the direction of the side of the sphere rotating with the free-stream flow (retreating side). The effect occurs due to the addition of momentum near the surface of the sphere, reducing the adverse pressure gradient on the retreating side which delays separation, whilst conversely increasing the adverse pressure gradient on the advancing side which promotes separation. The resultant pressure difference over the sphere produces a force in proportion to the Reynolds number and rotation ratio, $\alpha = \Omega D/(2U)$, with Ω the angular velocity, at least for small to moderate α. For certain flow conditions ($Re \sim 10^5$), a force in the opposite direction is generated; this is referred to as the 'negative' or 'inverse' Magnus effect. It is not expected that the inverse Magnus effect would be encountered over the Reynolds number range investigated in this study (Kim *et al.* 2014). Indeed, even for the normal Magnus effect, there has been little research conducted on it over the Reynolds number range of the current study. Notably, Tsuji, Morikawa & Mizuno (1985) collated past results in the range $Re < 1$ to $Re = 1.1 \times 10^5$ and conducted their own experiments over the range $5.50 \times 10^2 \leqslant Re \leqslant 1.60 \times 10^3$. In addition, various numerical studies (e.g. Giacobello, Ooi & Balachandar 2009; Poon *et al.* 2010; Dobson, Ooi & Poon 2014;

Rajamuni *et al.* 2018*b*) have documented the effect for $Re \leqslant 1000$. Over this relatively low Reynolds number range of the current study, and the range of rotation ratios implemented, it is expected that the lift force due to the Magnus effect will increase monotonically with increasing rotation ratio. As a result, for rotation at $\phi_{rot} = 0°$, the force from the Magnus effect is expected to be $90°$ out of phase with sphere transverse displacement, with the peak force occurring at $y/D = 0$ in the direction opposite to the motion of the sphere. Therefore, if the Magnus effect were to act in isolation, it is expected that the amplitude of sphere vibration would be reduced for $\phi_{rot} = 0°$.

Figure 4 shows key characteristics of the vibration response of the sphere for the four proportional gain values investigated at $\phi_{rot} = 0°$. Commencing with the mode I response, it is apparent from figure 4(*a*) that the imposed rotation alters the reduced velocity at which the vibration is instigated. As previously discussed, it is expected that the Magnus effect due to the imposed rotation would suppress vibration. However, increasing the proportional gain results in a reduction in the reduced velocity at which the vibration is instigated, down to $U^* = 4$ for $K_p^* = 4$, the largest proportional gain tested. Over this regime, the vibrations occur close to the natural frequency of the system (figure 4*b*), there is a sharp increase in the root-mean-square (r.m.s.) transverse force coefficient, C_y, where the vibration is instigated, as for the natural response (figure 4*c*), and the total phase remains close to that observed for the natural response (figure 4*d*).

Figure 5 shows sample time traces of the transverse displacement and force coefficient at $U^* = 4$ for the natural response and at $U^* = 5.25$ with imposed rotation ($K_p^* = 4$). As observed for the natural response in the mode I regime, with imposed rotation, the fluid force acting on the sphere is highly periodic and it is evident that the total phase is close to $0°$. The time trace and power spectral density (PSD) plots of the transverse force coefficient from figure 5 highlight the similarity between the two responses, suggesting the imposed rotation promotes early onset of the mode I response as opposed to a new mode of vibration. Furthermore, if the vibration was instigated due to a Magnus force like effect, then it would be expected that, as a minimum, an inflection in the trace of transverse force coefficient (figure 5*c*) would be observed at $y/D = 0$ where the Magnus effect is expected to be maximum. Rajamuni *et al.* (2018*b*) imposed constant rotation to a sphere constrained to one degree of freedom. They found that with the leading side of the sphere, in the transverse sense, rotating towards the oncoming free stream, the vortex street that developed either diminished in strength or was suppressed completely. Therefore, in this study, where for $\phi_{rot} = 0°$ the leading side of the sphere is always rotating towards the oncoming free stream, it was expected that the strength of the lift-inducing streamwise vortex structures would reduce. Rather, it is suspected that as the imposed rotation is linked to the system dynamics, periodic vortex shedding is promoted, enabling earlier onset and expansion of the resonance vibration regime.

At higher reduced velocities, perhaps the most notable feature of the amplitude response shown in figure 4(*a*), is that the imposed rotation results in an attenuation of the maximum vibration amplitude. For the proportional gain values investigated, a maximum reduction in the peak vibration amplitude of 44 % was observed. It is also evident that the peak amplitude response occurs at lower reduced velocities with increasing proportional gain and that higher proportional gain values are associated with a broader peak vibration region. Govardhan & Williamson (2005) showed that the mode II regime is associated with the total phase transitioning through $90°$. As can be seen in figure 4(*d*), the imposed rotation causes the total phase to transition from close
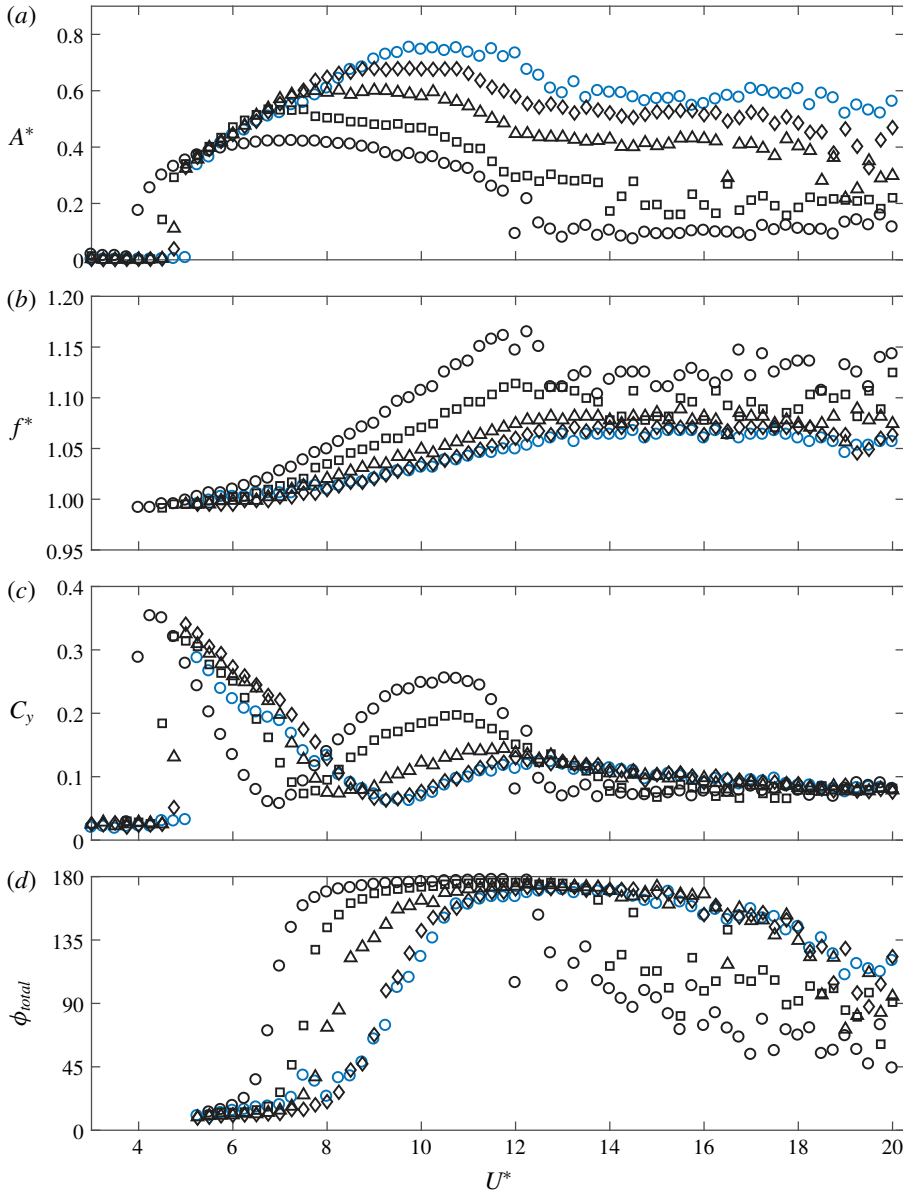
FIGURE 4. Response of the sphere with imposed rotation at $\phi_{rot} = 0°$ as a function of U^* for $K_p^* = 0.5, 1, 2$ and 4. (*a*) Variation of vibration amplitude, A^*. (*b*) Dominant vibration frequency obtained from the power spectrum of transverse sphere position. (*c*) Variation of the r.m.s. transverse force coefficient, C_y. (*d*) Variation of total phase, ϕ_{total}. ($\bigcirc$, blue) $K_p^* = 0$, ($\bigcirc$, black) $K_p^* = 4$, ($\square$) $K_p^* = 2$, ($\triangle$) $K_p^* = 1$, ($\diamond$) $K_p^* = 0.5$. Note that ϕ_{total} is presented in degrees.

to $0°$ through $90°$ at a lower reduced velocity. This, along with the decreased reduced velocity at peak vibration, implies that the mode II regime is shifted to increasingly lower reduced velocities with increasing proportional gain. Interestingly, the vibration
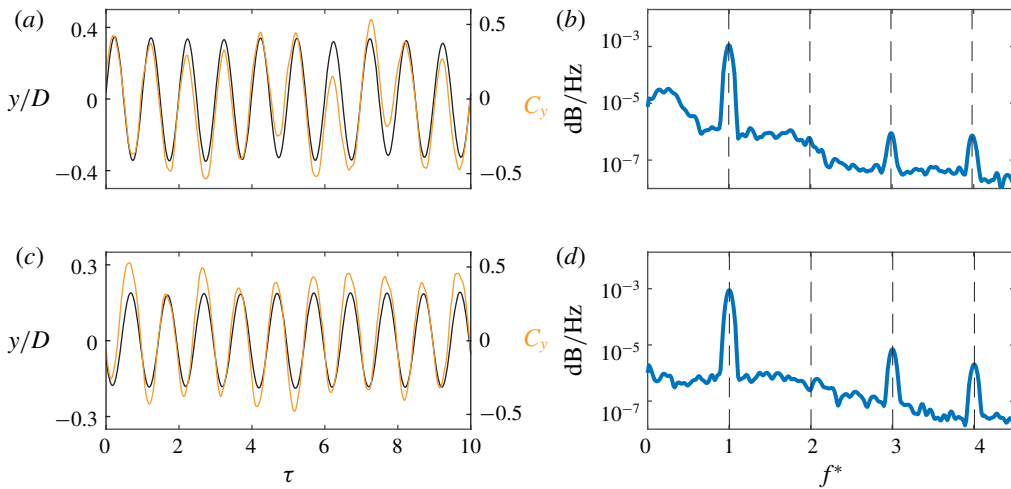
FIGURE 5. Variation in the characteristics of C_y with imposed rotation in the mode I regime. (*a*,*b*) Natural response at $U^* = 4$. (*c*,*d*) Response with $K_p^* = 4$ and $\phi_{rot} = 0°$ at $U^* = 5.25$. (*a*,*c*) Time traces of sphere displacement (black line) and C_y (orange line). The horizontal axis shows time non-dimensionalised by the oscillation period, $\tau = t/T$. (*b*,*d*) Power spectrum of C_y as a function of f^*. Black dashed lines represent the vibration frequency of the sphere and higher harmonics. Note that for (*a*,*c*) the scale of y/D and C_y has been adjusted for each plot to aid comparison.

frequency remains at $f^* \approx 1.03$ at the peak of the mode II response for all proportional gain values investigated (figure 4*b*).

For the sphere to undergo sustained vibration, there must be a net energy transfer from the fluid to the sphere over a vibration cycle. A net energy transfer can only occur with $0° < \phi_{total} < 180°$. For a given transverse force coefficient, the maximum energy transfer occurs with $\phi_{total} = 90°$, and reduces to zero at $\phi_{total} = 0°$ and $180°$. So increasing the proportional gain, which causes the total phase to transition closer to $\phi_{total} = 180°$ in the mode II regime, reduces the potential for net energy transfer to the sphere.

Over the range $4 \lesssim U^* \lesssim 12$, the imposed rotation noticeably alters the transverse force coefficient (figure 4*c*). The minimum in the transverse force coefficient, which is observed close to the peak of the mode II regime, remains almost constant for all proportional gain values. Past the peak of the mode II regime, there is a second maximum in the transverse force coefficient seen. The magnitude of the second maximum increases significantly with proportional gain. Considering the magnitude of the transverse force coefficient in conjunction with total phase, it is evident that the net energy transfer to the sphere remains relatively constant over a broad range of reduced velocities. This in turn may explain the relatively constant, and increasingly broad, peak vibration region seen with increasing proportional gain. Figure 6, which shows time traces of the transverse displacement and force coefficient at $U^* = 10$, for the natural response and with imposed rotation ($K_p^* = 4$), highlights how the imposed rotation continues to promote a highly periodic transverse force response past the mode I regime.

At $U^* \approx 12$, there is a distinct change in the response of the sphere for the largest proportional gain, $K_p^* = 4$, which is visible across the range of vibration
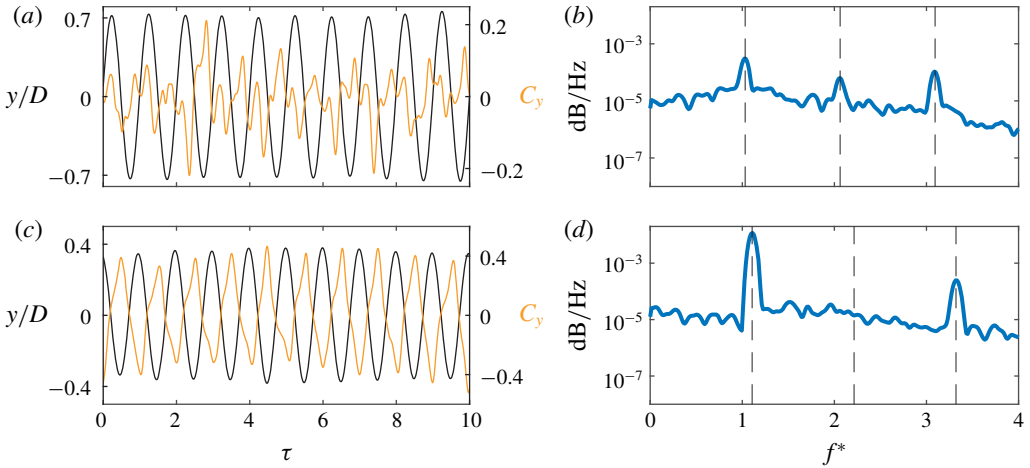
FIGURE 6. Variation in the characteristics of C_y with imposed rotation in the mode II regime ($U^* = 10$). (a,b) Natural response. (c,d) Response with $K_p^* = 4$ and $\phi_{rot} = 0°$. (a,c) Time traces of sphere displacement (black line) and C_y (orange line). The horizontal axis shows time non-dimensionalised by the oscillation period, $\tau = t/T$. (b,d) Power spectrum of C_y as a function of f^*. Black dashed lines represent the vibration frequency of the sphere and higher harmonics. Note that for (a,c) the scale of y/D and C_y has been adjusted for each plot to aid comparison.

characteristics examined in figure 4. Here, the steepest decline in vibration amplitude is observed (figure 4a), there is a step change in the vibration frequency (figure 4b), a rapid reduction in the transverse force coefficient (figure 4c) and, lastly, an abrupt reduction in total phase (figure 4d). It is conjectured that the periodicity promoted by the imposed rotation can no longer be sustained as the equivalent fixed-body (i.e. stationary sphere) vortex shedding frequency increases, moving further from the natural vibration frequency of the system. Consequently, the Magnus effect begins to dominate and the amplitude response is further reduced. In figure 4(d) it can be seen that total phase falls close to 90° at $U^* \approx 12$, and that it slowly decreases further at a similar rate to the natural response. In stark contrast to figures 5 and 6, figure 7 reveals a significantly decreased periodicity with imposed rotation.

Further to the reduction in periodicity of the transverse force as reduced velocity increases, a similar reduction is seen in the displacement response. To quantify this change, the definition of periodicity used by (Jauvtis *et al.* 2001) is adopted here. Periodicity is defined as $\mathcal{P} = \sqrt{2}y_{rms}/y_{max}$, noting it attains a value of unity for a purely sinusoidal signal and reduces in value for a less periodic signal. Figure 8 shows a reduction in the periodicity of the sphere displacement with imposed rotation at $\phi_{rot} = 0°$. When proportional gain is set to larger values, the magnitude of this reduction is increased and it begins to occur at lower reduced velocities.

In an effort to compare the magnitude of the imposed rotation to the open-loop control studies of Sareen *et al.* (2018a,b), the mean effective velocity ratio, $\alpha_r^* = \Omega_{max}D/(2U)$, where Ω_{max} is the maximum angular velocity over a vibration cycle, was calculated. As can be observed from figure 9, a significant benefit of the feedback control is that as the amplitude of imposed rotation is linked to the sphere displacement; when the vibrations are suppressed, the amplitude of the imposed rotation reduces in proportion. Consequently, past the peak of mode II, where the
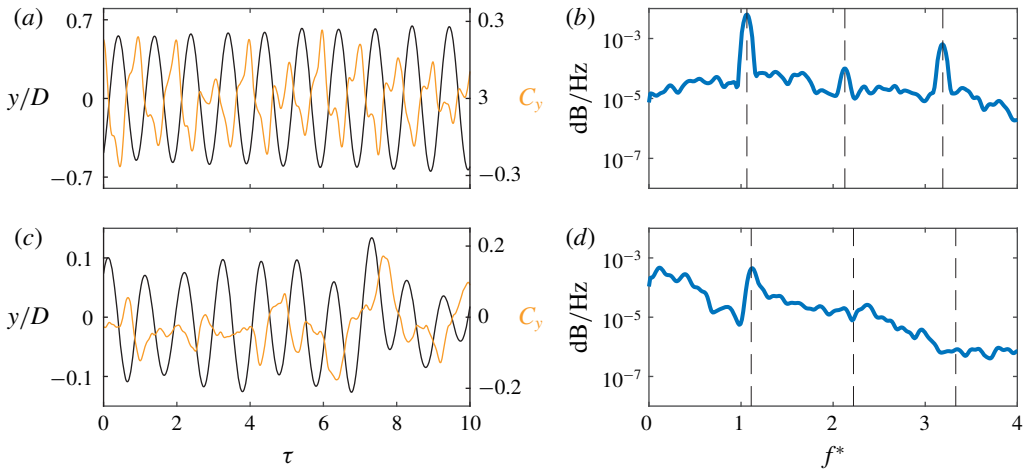
FIGURE 7. Variation in the characteristics of C_y with imposed rotation in the mode III transition regime ($U^* = 13$). (a,b) Natural response. (c,d) Response with $K_p^* = 4$ and $\phi_{rot} = 0°$. (a,c) Time traces of sphere displacement (black line) and C_y (orange line). The horizontal axis shows time non-dimensionalised by the oscillation period, $\tau = t/T$. (b,d) Power spectrum of C_y as a function of f^*. Black dashed lines represent the vibration frequency of the sphere and higher harmonics. Note that for (a,c) the scale of y/D and C_y has been adjusted for each plot to aid comparison.
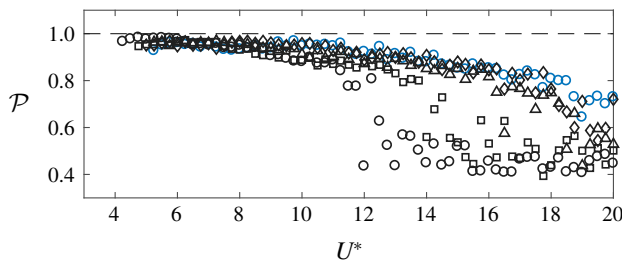
FIGURE 8. Periodicity of the sphere displacement as a function of U^*. (○, blue) $K_p^* = 0$, (○, black) $K_p^* = 4$, (□) $K_p^* = 2$, (△) $K_p^* = 1$, (◇) $K_p^* = 0.5$. The dashed line represents a purely sinusoidal signal.

vibrations are significantly suppressed, the largest proportional gain value investigated, $K_p^* = 4$, has a very small effective velocity ratio ($\alpha_r^* < 0.1$).

3.2. *Control imposed with a rotation phase of* 180°

As may be expected, the amplitude response for $\phi_{rot} = 180°$ is loosely inverse to that for $\phi_{rot} = 0°$. Overall, there is a slightly delayed instigation of the vibration for large proportional gains, an attenuation of vibration in the mode I regime and a monotonic increase from near the peak of the mode II regime onwards.

Figure 10 shows key characteristics of the vibration response of the sphere with $\phi_{rot} = 180°$ for the four proportional gain values investigated. The amplitude response of the sphere is shown in figure 10(a). For the natural response, the vibration commences suddenly at $U^* = 5.25$, with the amplitude of vibration increasing from
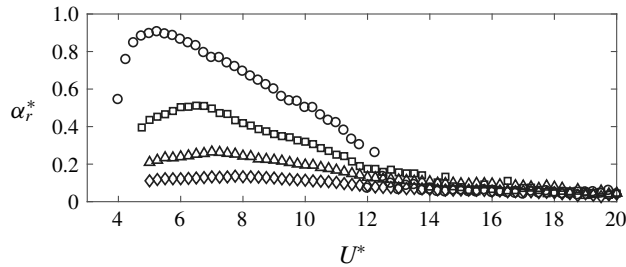
FIGURE 9. Mean velocity ratio, α_r^*, as a function of U^*. (○) $K_p^* = 4$, (□) $K_p^* = 2$, (△) $K_p^* = 1$, (◇) $K_p^* = 0.5$.

$A^* = 0$ to $A^* = 0.37$. With increasing proportional gain, the magnitude of the initial vibration is increasingly attenuated. For the highest proportional gain tested, $K_p^* = 4$, the vibration response increases slowly, and relatively linearly, up to $U^* = 8.5$. For $U^* \lesssim 9$, the total phase remains close to $0°$ for all proportional gain values (figure 10d), although there is a significant variation in the transverse force coefficient as shown in figure 10(c). Over this regime, as shown in figure 10(b), the vibration frequency is reduced, particularly for $K_p^* = 4$.

As discussed in § 3.1, at low reduced velocities it appears that the imposed rotation promotes a highly periodic transverse force signal. For $\phi_{rot} = 0°$, this in turn resulted in highly periodic vibration. However, it was noted that the vibration was not anticipated given the expected direction of the Magnus effect. Here, for $\phi_{rot} = 180°$, it was expected that the Magnus effect would contribute to increased vibration. Evidently, this did not occur. As can be seen from figure 11, the imposed rotation results in a highly periodic, albeit attenuated, transverse force signal. The combination of attenuated transverse force and shift in total phase closer to $0°$, results in a reduction in the net energy transfer to the sphere over a vibration cycle in the mode I regime.

Whereas for $\phi_{rot} = 0°$ and $K_p^* = 4$, $U^* \approx 12$ marked a change in the characteristics of the vibration response, for $\phi_{rot} = 180°$, $U^* \approx 9$ marks a distinct change in the response for all proportional gain values. At $U^* \approx 9$, prior to the peak of the mode II response seen with no imposed rotation, the amplitude of vibration for all proportional gain values investigated switches from an attenuated to an amplified response. Here, $U^* \approx 9$ coincides with the sharp increase in total phase seen for the natural response. From $U^* \approx 9$, for $K_p^* \geqslant 1$, the vibration response increases monotonically well above the amplitude observed with no imposed rotation. A similar trend was observed for a sphere (Sareen *et al.* 2018b) and circular cylinder (Zhao *et al.* 2018) with imposed open-loop rotary oscillations, and for a circular cylinder with feedback control (Vicente-Ludlam *et al.* 2018). This type of response has been labelled as 'rotation-induced' vibration, a result of the imposed rotation dominating the natural vortex shedding, causing a 'galloping-like' response. It is evident from figure 12 that over the rotation-induced vibration regime, the periodicity of the vibration approaches unity as proportional gain is increased.

As shown in figure 13, for $U^* \lesssim 9$, the frequency spectrum of transverse force consists of a single distinct peak at $f_{C_y}^* = 1$. Above $U^* \approx 9$, harmonics of f^* begin to appear, and by $U^* = 20$ the spectrum is dominated by vibration at $f^* = 3$. Figure 14 highlights how the frequency response of the transverse force coefficient is dominated by the second harmonic of vibration frequency at $U^* = 20$.
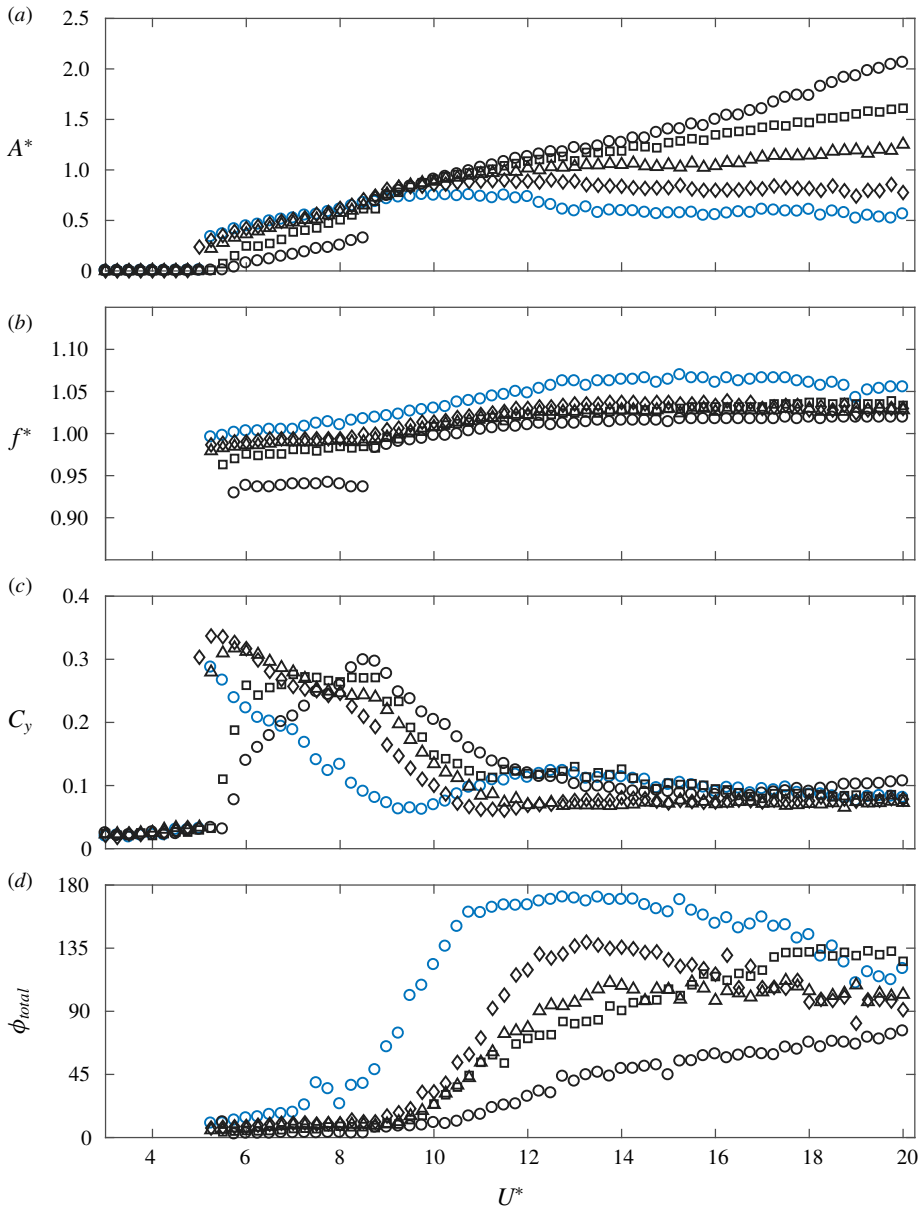
FIGURE 10. Response of the sphere with imposed rotation at $\phi_{rot} = 180°$ as a function of U^* for $K_p^* = 0.5, 1, 2$ and 4. (*a*) Variation of vibration amplitude, A^*. (*b*) Dominant vibration frequency obtained from the power spectrum of transverse sphere position. (*c*) Variation of the r.m.s. transverse force coefficient, C_y. (*d*) Variation of total phase, ϕ_{total}. (○, blue) $K_p^* = 0$, (○, black) $K_p^* = 4$, (□) $K_p^* = 2$, (△) $K_p^* = 1$, (◇) $K_p^* = 0.5$. Note that ϕ_{total} is presented in degrees.

As can be seen from figure 10(*b*), there is minimal variation in the vibration frequency for $\phi_{rot} = 180°$. Vicente-Ludlam *et al.* (2018) reported that for the circular cylinder, the imposed feedback control resulted in the vibration frequency remaining
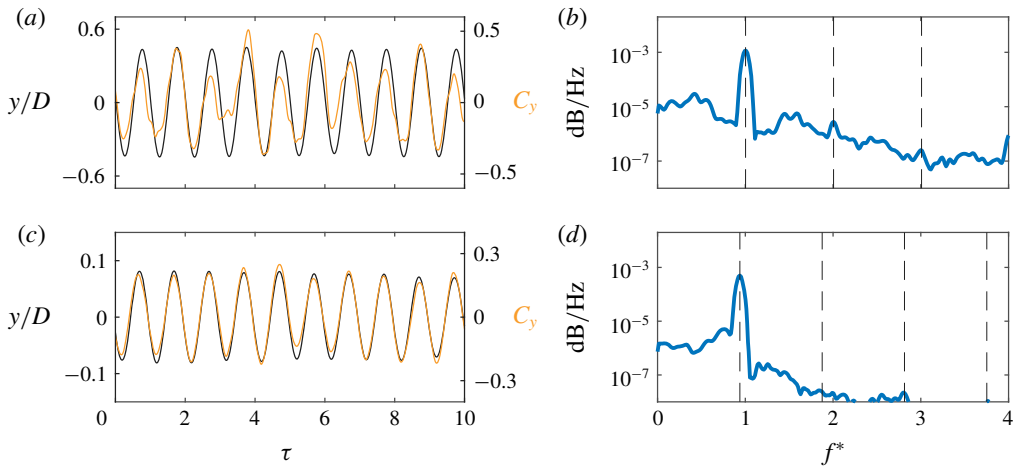
FIGURE 11. Variation in the characteristics of C_y with imposed rotation in the mode I regime ($U^* = 6$). (*a,b*) Natural response. (*c,d*) Response with $K_p^* = 4$ and $\phi_{rot} = 180°$. (*a,c*) Time traces of sphere displacement (black line) and C_y (orange line). The horizontal axis shows time non-dimensionalised by the oscillation period, $\tau = t/T$. (*b,d*) Power spectrum of C_y as a function of f^*. Black dashed lines represent the vibration frequency of the sphere and higher harmonics. Note that for (*a,c*) the scale of y/D and C_y has been adjusted for each plot to aid comparison.
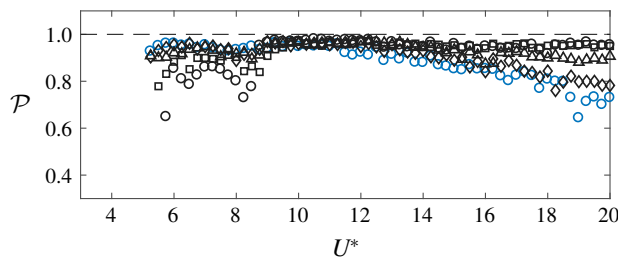

FIGURE 12. Periodicity of the sphere displacement as a function of U^*. ($\bigcirc$, blue) $K_p^* = 0$, ($\bigcirc$, black) $K_p^* = 4$, ($\square$) $K_p^* = 2$, ($\triangle$) $K_p^* = 1$, ($\diamondsuit$) $K_p^* = 0.5$. The dashed line represents a purely sinusoidal signal.

constant close to $f^* = 1$ in the rotation-induced vibration regime. Likewise, for $\phi_{rot} = 180°$, above $U^* \approx 9$ where rotation-induced vibration is observed, the vibration frequency remained close to constant, slightly below that observed for the natural response. Over this regime, where the vibration response was amplified, the total phase progressively deviates from the trend seen for the natural response as proportional gain increases (figure 10*d*). For $K_p^* = 4$, the total phase increases monotonically up to $\phi_{total} = 76°$ at $U^* = 20$.

Once again, comparing the velocity ratio values to those for open-loop rotary control (Sareen *et al.* 2018*a*), we find that the feedback control provides a more efficient means to amplify the vibration (figure 15). Whilst not directly attempting to optimise the amplification of vibration, Sareen *et al.* (2018*a*) did present results with imposed rotary oscillations at a frequency 1.1 times the natural frequency of the system with $\alpha_r^* = 1$, resulting in a vibration amplitude of $A^* = 1$ at $U^* = 20$. Here,
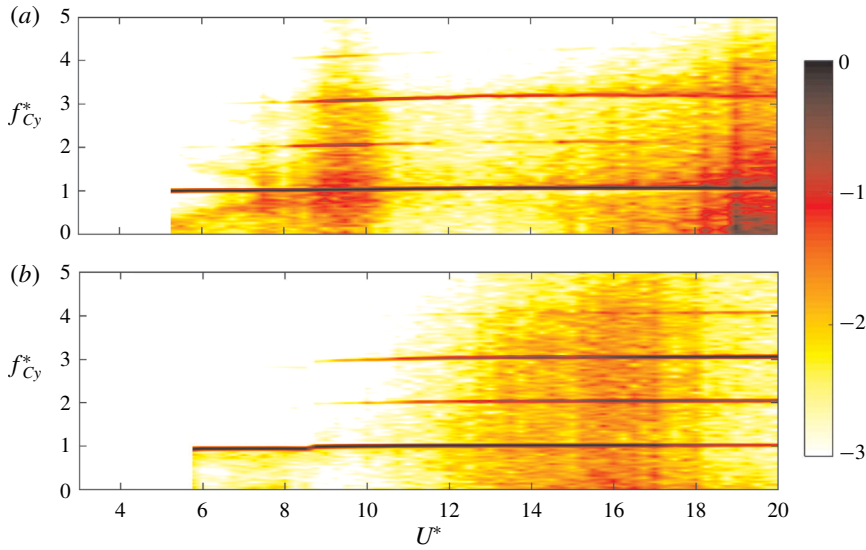
FIGURE 13. Frequency PSD contour plots of C_y against U^*. (*a*) Natural response; (*b*) $\phi_{rot} = 180°$ and $K_p^* = 4$. The spectral power is normalised by the maximum value at each U^* and is presented on a $\log_{10}$ scale.
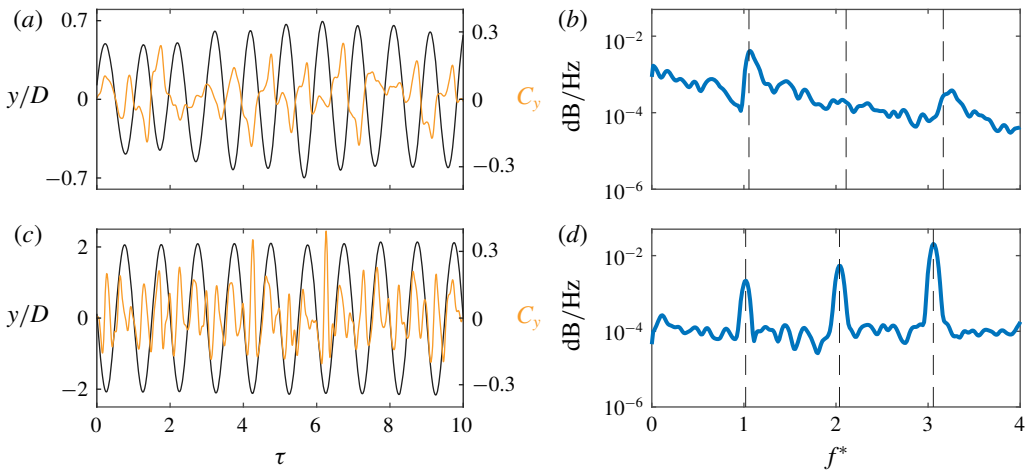

FIGURE 14. Variation in the characteristics of C_y with imposed rotation in the mode III transition regime ($U^* = 20$). (*a,b*) Natural response. (*c,d*) Response with $K_p^* = 4$ and $\phi_{rot} = 180°$. (*a,c*) Time traces of sphere displacement (black line) and C_y (orange line). The horizontal axis shows time non-dimensionalised by the oscillation period, $\tau = t/T$. (*b,d*) Power spectrum of C_y as a function of f^*. Black dashed lines represent the vibration frequency of the sphere and higher harmonics. Note that for (*a,c*) the scale of y/D and C_y has been adjusted for each plot to aid comparison.

we have two comparable data points at $U^* = 20$; imposed rotation with $K_p^* = 2$ and $\alpha_r^* = 0.51$ resulting in $A^* = 1.27$, and imposed rotation with $K_p^* = 4$ and $\alpha_r^* = 1.30$ resulting in $A^* = 2.1$.
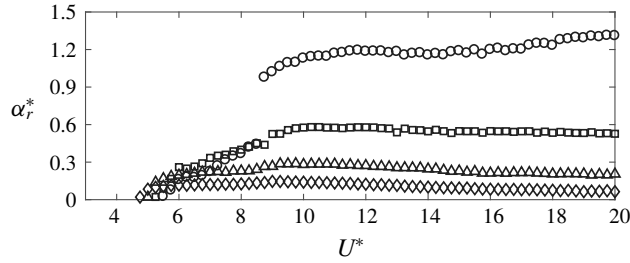
FIGURE 15. Mean amplitude ratio, α_r^*, as a function of U^*. ($\bigcirc$) $K_p^* = 4$, ($\square$) $K_p^* = 2$, ($\triangle$) $K_p^* = 1$, ($\diamondsuit$) $K_p^* = 0.5$.

3.3. *Effect of phase variation*

In §§ 3.1 and 3.2, the effect of rotation at $\phi_{rot} = 0°$ and $\phi_{rot} = 180°$ was examined. It was shown that varying the rotation phase significantly altered the vibration response of the sphere. To determine how the vibration response evolves over the range $0° \leqslant \phi_{rot} \leqslant 360°$, in this section the second control law (2.5) is implemented. In this study, the rotation phase is varied in $15°$ increments for $K_p^* = 0.5$, 1, 2 and 4 at reduced velocities of $U^* = 6$, 10 and 14 corresponding to mode I, mode II and mode III transition regimes for the non-rotating sphere.

3.3.1. *Mode I*

Figure 16 shows key characteristics of the vibration response of the sphere for the four proportional gain values investigated over the range $0° \leqslant \phi_{rot} \leqslant 360°$ at $U^* = 6$. The amplitude response of the sphere is plotted in figure 16(*a*). Due to the complex response over $90° \leqslant \phi_{rot} \leqslant 180°$, measurements were acquired in $5°$ increments in this range. For all proportional gain values investigated there is no amplification of the vibration amplitude. For $K_p^* \leqslant 1$ there is a moderate reduction in the amplitude response over the range $150° \lesssim \phi_{rot} \lesssim 360°$. For larger gain values, $K_p^* \geqslant 2$, there is significant variation in the vibration response over the full range of rotation phase. The maximum response for $K_p^* \geqslant 2$ is seen close to $\phi_{rot} \approx 0°$, with the minimum, a reduction of up to 97 % for $K_p^* = 4$, observed between $90° \lesssim \phi_{rot} \lesssim 165°$.

Coincidentally, the choice of $K_p^* = 2$ reveals a highly sensitive region of the vibration response. For $K_p^* = 2$, a 'lobe' can be observed between approximately $120° \lesssim \phi_{rot} \lesssim 150°$. Within this lobe the vibration is only moderately suppressed, whilst to each side of the lobe, the vibration is nearly completely suppressed. Further testing over this region, not presented here, revealed that particularly for $90° \lesssim \phi_{rot} \lesssim 120°$ and to a lesser extent for $150° \lesssim \phi_{rot} \lesssim 170°$, the amplitude response takes a significant time to stabilise. Over the vast majority of the parameter space examined in this study, the vibration typically stabilised within one minute ($\sim$16 vibration cycles). However, over this sensitive region the vibrations took approximately ten minutes ($\sim$162 vibration cycles) to stabilise. Over $90° \lesssim \phi_{rot} \lesssim 150°$ the amplitude of vibration varied significantly with small changes in K_p^*. At $\phi_{rot} \approx 105°$ the vibration was most sensitive between $1.75 \lesssim K_p^* \lesssim 2$. This rose to $2 \lesssim K_p^* \lesssim 2.25$ for $\phi_{rot} \approx 135°$, and fell to $1.5 \lesssim K_p^* \lesssim 1.75$ for $\phi_{rot} \approx 150°$.

For $K_p^* \leqslant 2$ there is minimal variation in the vibration frequency (figure 16*b*). For $K_p^* = 4$, however, there is a step change in the vibration frequency at $\phi_{rot} = 135°$, which occurs over the region where the lobe is observed in the amplitude response.
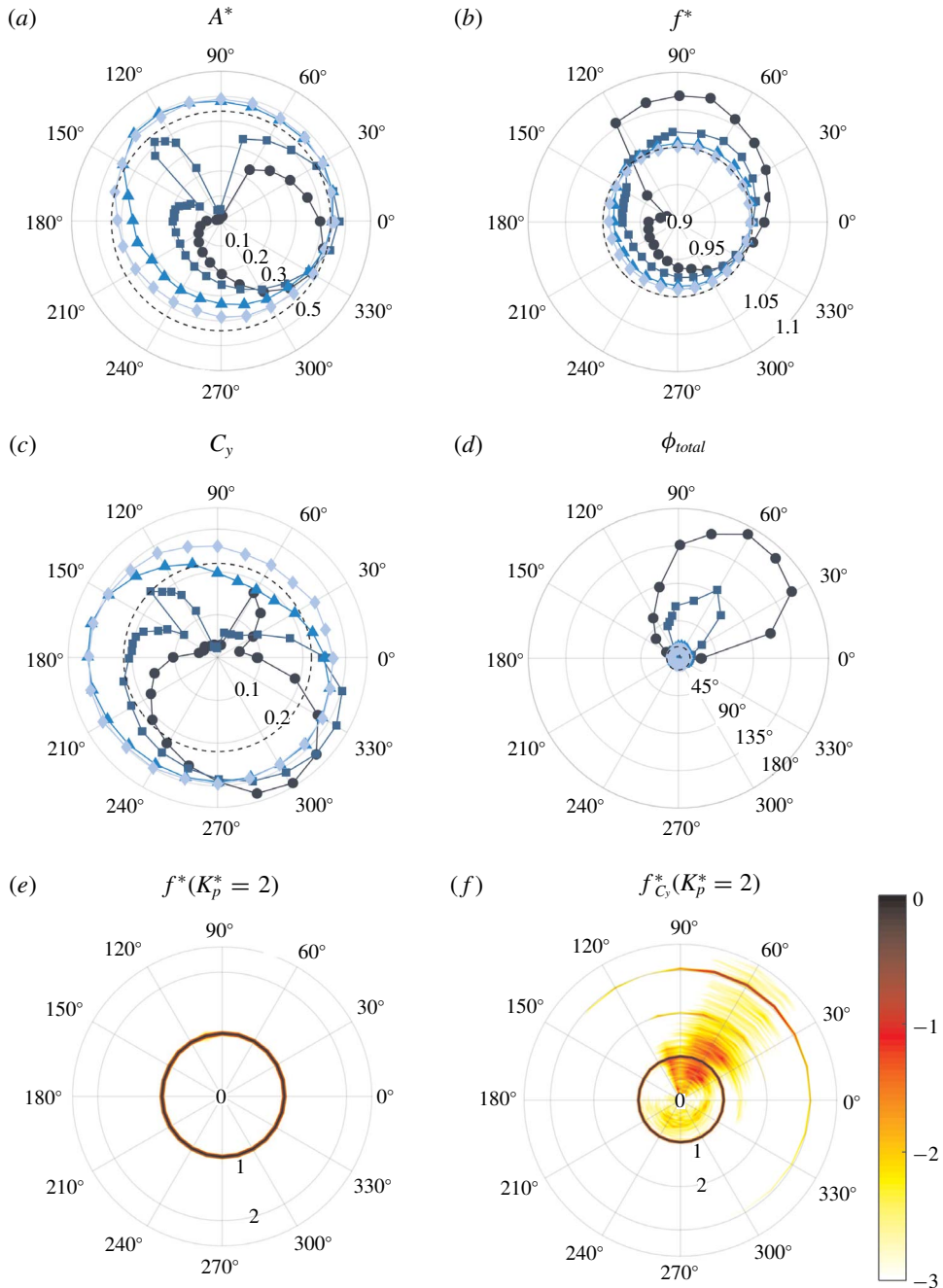
FIGURE 16. Response of the sphere in the mode I regime ($U^* = 6$) with imposed rotation over the range $0° \leqslant \phi_{rot} \leqslant 360°$ (polar angle) for four proportional gain values $K_p^* = 0.5, 1, 2$ and 4. Radius shows (*a*) A^*, (*b*) f^*, (*c*) C_y and (*d*) ϕ_{total}. In (*a*–*d*) (●) $K_p^* = 4$, (■) $K_p^* = 2$, (▲) $K_p^* = 1$, (◆) $K_p^* = 0.5$. (*e,f*) PSD contour plots of f^* and $f_{C_y}^*$, respectively, for $K_p^* = 2$. The spectral power is normalised by the maximum value at each ϕ_{rot} and is presented on a $\log_{10}$ scale. The black dashed line represents the natural response.

For $K_p^* \geqslant 2$, figure 16(c) shows a point of relatively sharp change in the magnitude of the transverse force coefficient. This point occurs at $\phi_{rot} = 135°$ for $K_p^* = 2$, and $\phi_{rot} = 60°$ for $K_p^* = 4$, where a corresponding sharp change in amplitude response was observed. Figure 16(d) reveals a consistent pattern in the variation of total phase. For all proportional gain values investigated, the maximum total phase is located at 60°. From approximately $150° \lesssim \phi_{rot} \lesssim 330°$, total phase is reduced below that observed for the natural response. Whilst this pattern was consistent for all proportional gain values tested, at least from examination of the data obtained, there appears to be correlation between changes in total phase, C_y, and the amplitude response in this instance as one might expect.

Figure 16(e,f) shows PSD contour plots of the frequency of sphere transverse displacement and transverse force respectively. Over the region of amplitude sensitivity, $120° \lesssim \phi_{rot} \lesssim 150°$, for $K_p^* = 2$, the vibrations remain periodic with the spectral power concentrated close to the natural frequency of the system. Similarly, the spectral power of transverse force remains highly periodic over the central portion of the sensitive region, with a broader frequency response seen at $\phi_{rot} = 105°$. Figure 16(f) also reveals a broad range of spectral power for the transverse force, centralised around $\phi_{rot} = 60°$ where significant changes in total phase were observed in figure 16(d).

3.3.2. *Mode II*

Previous studies implementing open-loop control for a sphere undergoing VIV have found it most difficult to alter the vibration response at the peak of the mode II regime (Sareen *et al.* 2018a,b). Figure 17 shows the response of the sphere with imposed rotation in the mode II regime ($U^* = 10$). The imposed rotation results in a slight increase in the vibration amplitude, for all proportional gain values, over the range $165° \lesssim \phi_{rot} \lesssim 300°$ (figure 17a). Conversely, the vibrations are attenuated between $315° \lesssim \phi_{rot} \lesssim 135°$. The maximum attenuation for all proportional gain values is observed at $\phi_{rot} \approx 60°$. It is not immediately obvious why this maximum attenuation occurs at this phase angle. Here, the transverse force is only slightly attenuated over the region $45° \lesssim \phi_{rot} \lesssim 120°$ (figure 17c). Additionally, there is no clear trend in total phase suggesting a particular amplitude response (figure 17d). At $\phi_{rot} \approx 60°$, for $K_p^* \geqslant 2$, the total phase is reduced well below that for the natural response, whilst for $K_p^* \leqslant 1$, total phase is increased.

As can be seen from figure 17(e), for $K_p^* = 4$, where the vibrations are amplified, the spectral power is concentrated at $f^* = 1$. Whilst, where the vibrations are attenuated, the spectral power is distributed broadly over the range $0 \lesssim f^* \lesssim 2$. Similarly, distinct differences in the frequency spectra of transverse force signals for the regimes of vibration amplification and attenuation can be observed in figure 17(f). Interestingly, where the vibrations are attenuated, there is a distinct lack of spectral power at $f_{C_y}^* = 1$. Conversely, where the vibration is amplified, there is a strong peak in spectral power at $f_{C_y}^* = 1$ and to a lesser extent, peaks at $f_{C_y}^* = 2$ and $f_{C_y}^* = 3$.

3.3.3. *Mode III*

In the mode III transition regime, a similar response in the vibration amplitude to that seen in the mode II regime can be observed, although, in the mode III transition regime a more pronounced trend is seen. The vibration is amplified over $150° \lesssim \phi_{rot} \lesssim 315°$, and attenuated elsewhere as observed in figure 18(a), with the peak vibration amplitude occurring between $180° \leqslant \phi_{rot} \leqslant 210°$. The vibration frequency (figure 18b), and transverse force coefficient (figure 18c), also show similar trends to the mode II
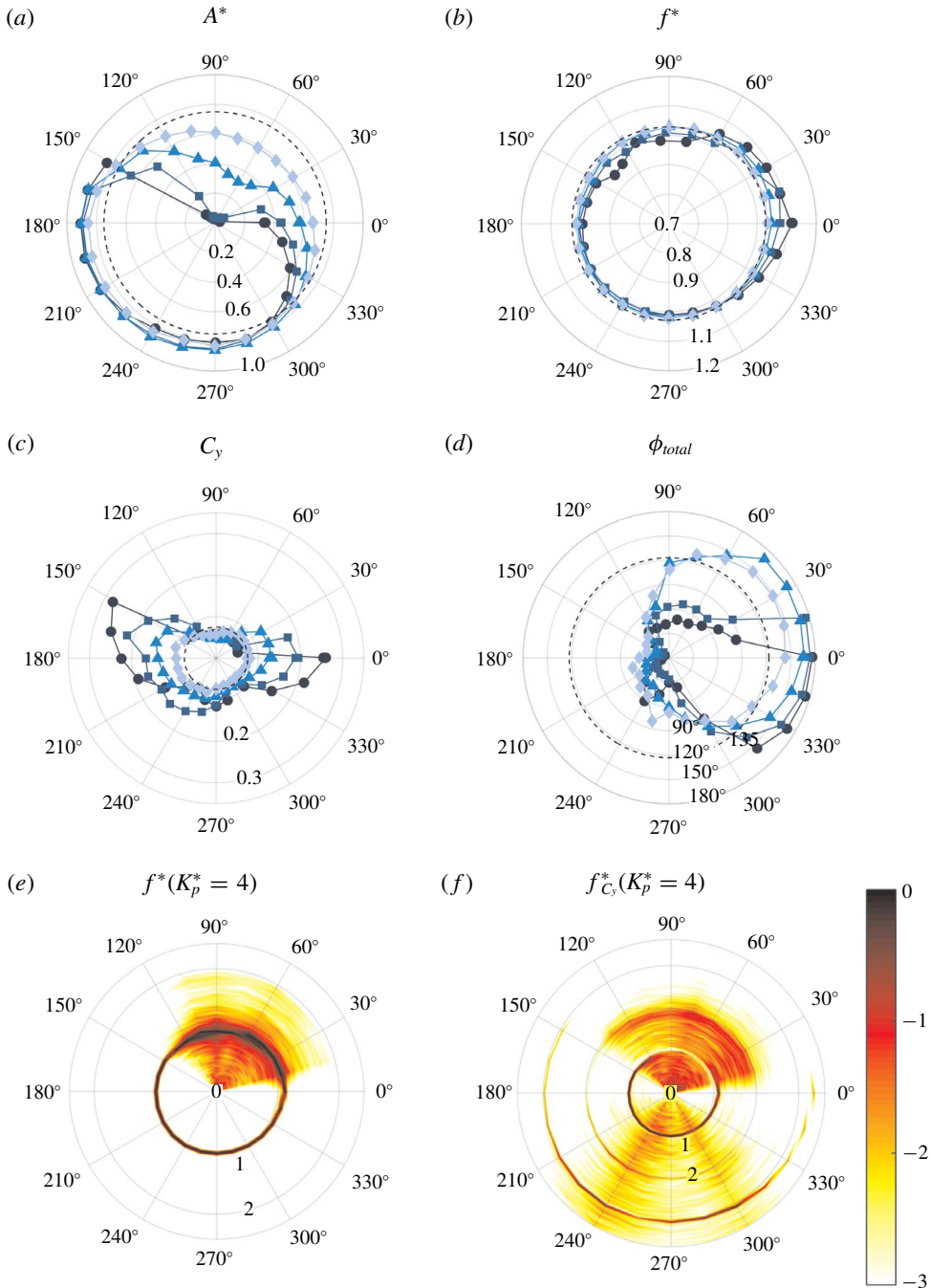
FIGURE 17. Response of the sphere in the mode II regime ($U^* = 10$) with imposed rotation over the range $0° \leqslant \phi_{rot} \leqslant 360°$ for four proportional gain values $K_p^* = 0.5, 1, 2$ and 4. Radius shows (*a*) A^*, (*b*) f^*, (*c*) C_y and (*d*) ϕ_{total}. In (*a–d*) (●) $K_p^* = 4$, (■) $K_p^* = 2$, (▲) $K_p^* = 1$, (◆) $K_p^* = 0.5$. (*e,f*) PSD contour plots of f^* and $f_{C_y}^*$, respectively, for $K_p^* = 4$. The spectral power is normalised by the maximum value at each ϕ_{rot} and is presented on a $\log_{10}$ scale. The black dashed line represents the natural response.

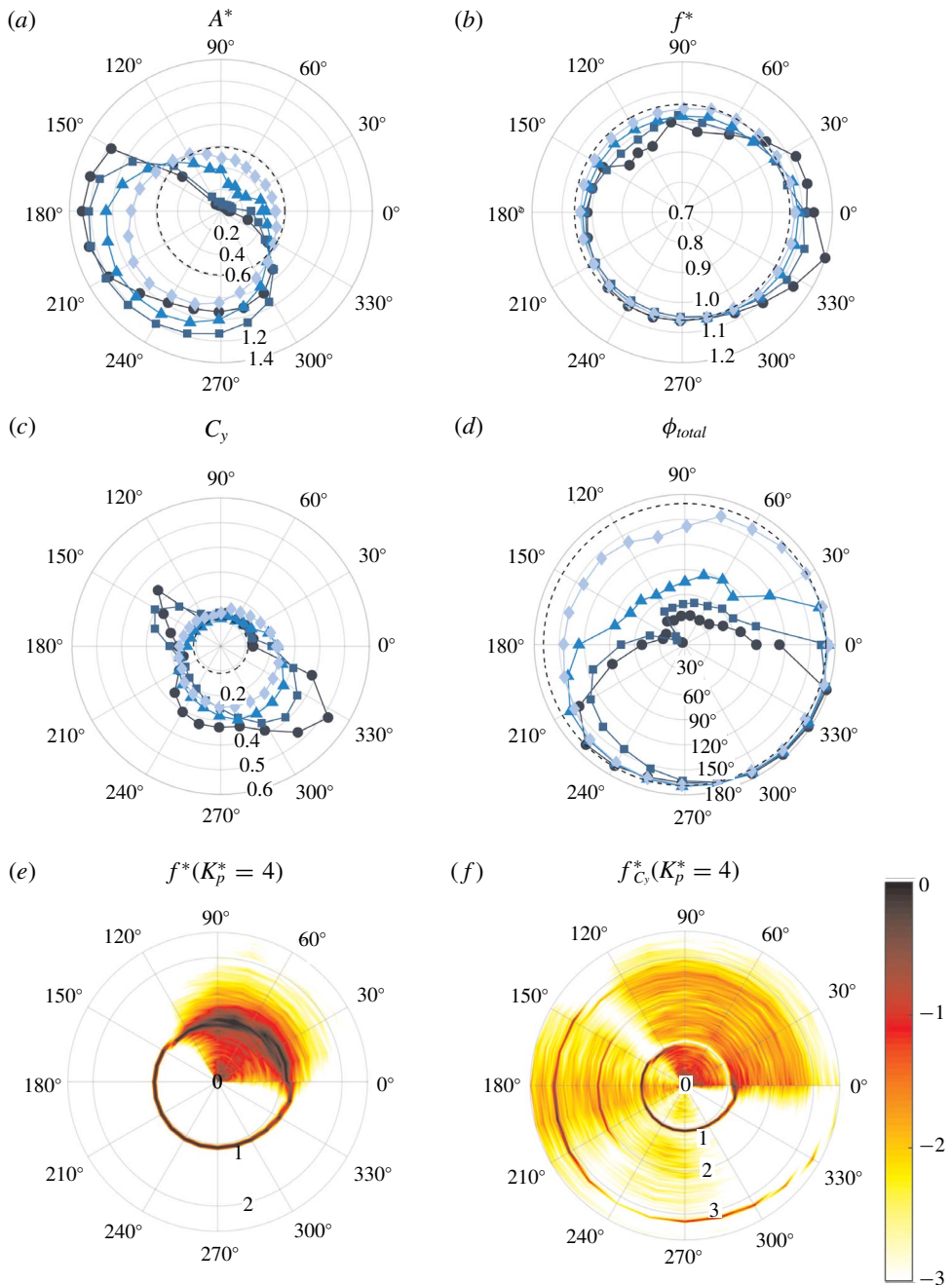FIGURE 18. Response of the sphere in the mode III transition regime ($U^* = 14$) with imposed rotation over the range $0° \leqslant \phi_{rot} \leqslant 360°$ for four proportional gain values $K_p^* = 0.5, 1, 2$ and 4. Radius shows (*a*) A^*, (*b*) f^*, (*c*) C_y and (*d*) ϕ_{total}. In (*a–d*) (●) $K_p^* = 4$, (■) $K_p^* = 2$, (▲) $K_p^* = 1$, (◆) $K_p^* = 0.5$. (*e,f*) PSD contour plots of f^* and $f_{C_y}^*$, respectively, for $K_p^* = 2$. The spectral power is normalised by the maximum value at each U^* and is presented on a $\log_{10}$ scale. The black dashed line represents the natural response.

regime. However, there are marked differences in total phase, perhaps unsurprisingly given the variation in total phase between the two regimes for the natural response. Here, total phase remains close to the natural response, $\phi_{total} \approx 170°$, over $210° \lesssim \phi_{rot} \lesssim 345°$, and is reduced elsewhere with short transition regions ($\sim 30°$) for large proportional gains.

Figure 18(e) reveals a similar trend in vibration frequency to that seen in the mode II regime for $K_p^* = 4$, although with an increased spread in spectral power where the vibration is suppressed. Once more, as for the mode II regime, there is a distinct lack of spectral power at $f_{C_y}^* = 1$ where vibration is suppressed, and peaks in spectral power evident close to $f_{C_y}^* = 2$ and $f_{C_y}^* = 3$ over much of the region where the vibration is amplified.

3.4. *Wake structures*

As first illustrated by Govardhan & Williamson (2005), and recently elucidated in great detail by Eshbal *et al.* (2019), the vibration of an elastically mounted sphere is primarily a result of the formation of two counter-rotating streamwise vortices. Several studies employing extensive PIV measurements of tethered spheres have further revealed the intricate aspects of fluid motion that lead to sustained vibration. In particular, the influence of the separating shear layer and weaker secondary vortices, in conjunction with sphere motion, on the overall wake structure has been detailed (van Hout, Krakovich & Gottlieb 2010; Eshbal, Krakovich & van Hout 2012; Krakovich, Eshbal & van Hout 2013; van Hout, Katz & Greenblatt 2013b). In the regime where large-amplitude vibration occurs, interaction between near wake vortices, the sphere, and the separating shear layer was found to lead to pinch-off of the dominant streamwise vortex structures. Krakovich *et al.* (2013) estimated the fluid force acting on the sphere using the analogy between the two counter-rotating streamwise vortices seen here and wing-tip vortices in the wake of an aircraft. Comparable results were obtained, highlighting the importance of these dominant structures in sustaining vibration. Whilst evidently, the problem is strongly three-dimensional and dynamic in nature, here, phase-averaged PIV has been employed in the transverse (*y*–*z*) and equatorial (*x*–*y*) planes to reveal the effect of the imposed rotation on the timing of the dominant streamwise vortex structures that have been shown to be the primary contributor to sustained vibration. PIV in the transverse plane, located at $x/D = 1.5$, reveals the development of streamwise vorticity over a vibration cycle. PIV in the equatorial plane offers further insight into how the imposed rotation alters the position of the wake structures in relation to the sphere.

When the imposed rotation nearly completely suppresses vibration, the wake resembles that of a fixed sphere, which over the Reynolds number range tested in this study ($3900 \lesssim Re \lesssim 25\,800$), consists of vortices that shed at random azimuth angles each shedding cycle (Sakamoto & Haniu 1990) (note that due to the presence of the mounting rod, there will be a bias to vortex shedding at particular azimuths as discussed in §2.2). As a result, the phase-averaged PIV acquired in the *y*–*z* plane in this study does not reveal the streamwise vortex structures for significantly suppressed vibration. Therefore, in this section, representative cases in the mode II and mode III transition regimes, where sufficient vibration exists to reveal the streamwise vortex structures, are examined to highlight changes in wake structure due to the imposed rotation.

Figure 19 shows streamwise vorticity in the mode II regime with no imposed rotation, and two representative cases of imposed rotation at $\phi_{rot} = 0°$ and $\phi_{rot} = 180°$,
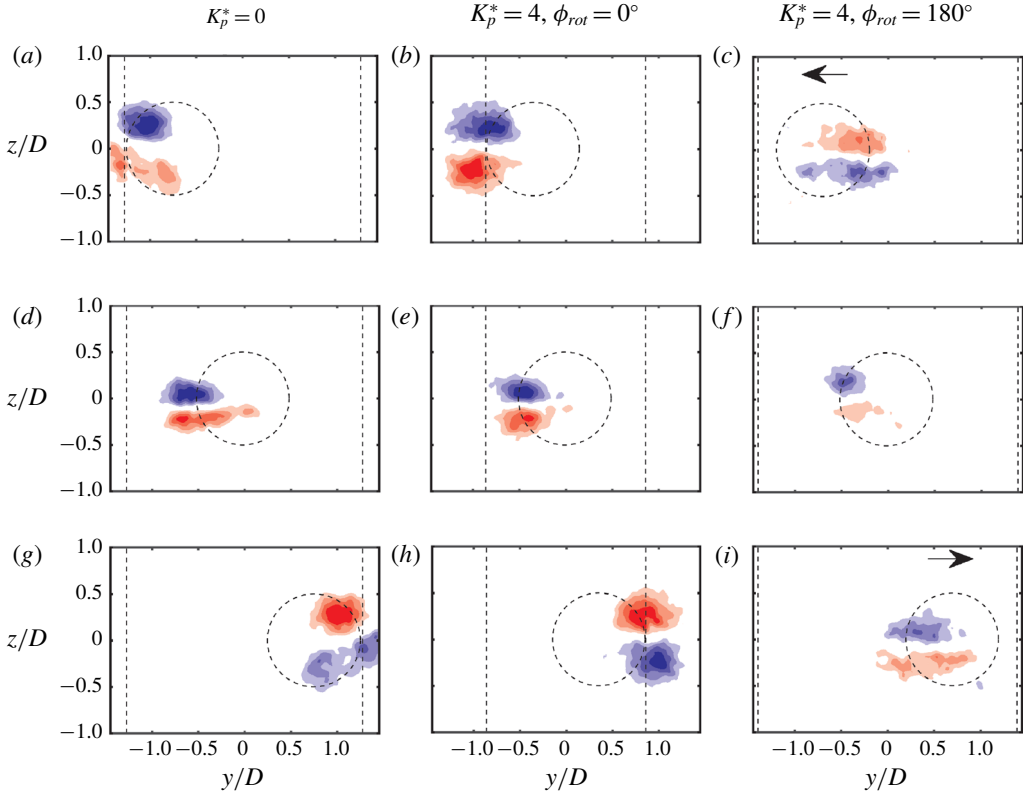
FIGURE 19. Streamwise vorticity shown in the cross-stream plane at $x/D = 1.5$ in the mode II regime ($U^* = 10$). (*a,d,g*) $K_p^* = 0$. (*b,e,h*) $K_p^* = 4$, $\phi_{rot} = 0°$. (*c,f,i*) $K_p^* = 4$, $\phi_{rot} = 180°$. From top to bottom, each plot is separated by approximately a quarter period. The vertical black dashed lines show the extremities of sphere displacement. The black dashed circle shows the sphere location. The black arrows indicate the direction of motion. Blue and red contours show clockwise and anti-clockwise vorticity respectively. The normalised vorticity, $\omega^* = \omega D/U$, is depicted by the colour map over eight steps in the range $\omega^* \in [-2, 2]$.

with $K_p^* = 4$. The sphere location, which has been approximately adjusted allowing for the time for the streamwise vortex structures to convect to the imaging plane, is depicted by a dashed black circle outline. The extremities of sphere motion are depicted by vertical black dashed lines. For $K_p^* = 4$ and $\phi_{rot} = 180°$, vorticity has not been presented at the extremity of sphere displacement due to the minimal vorticity seen at these locations. Positions highlighting maximum vorticity were chosen instead. In these instances, the black arrows depict the direction of sphere motion. For the three cases illustrated in figure 19, it can be observed that with imposed rotation the wake still primarily consists of the counter-rotating vortex pair seen for the natural response. There are, however, changes to the spatial position and timing of these vortices.

It is difficult to make detailed observations about the strength and shape of vortex structures due to the phase-averaging process. Increasing vibration amplitude results in vorticity been averaged over a greater range of sphere displacement values. As a result
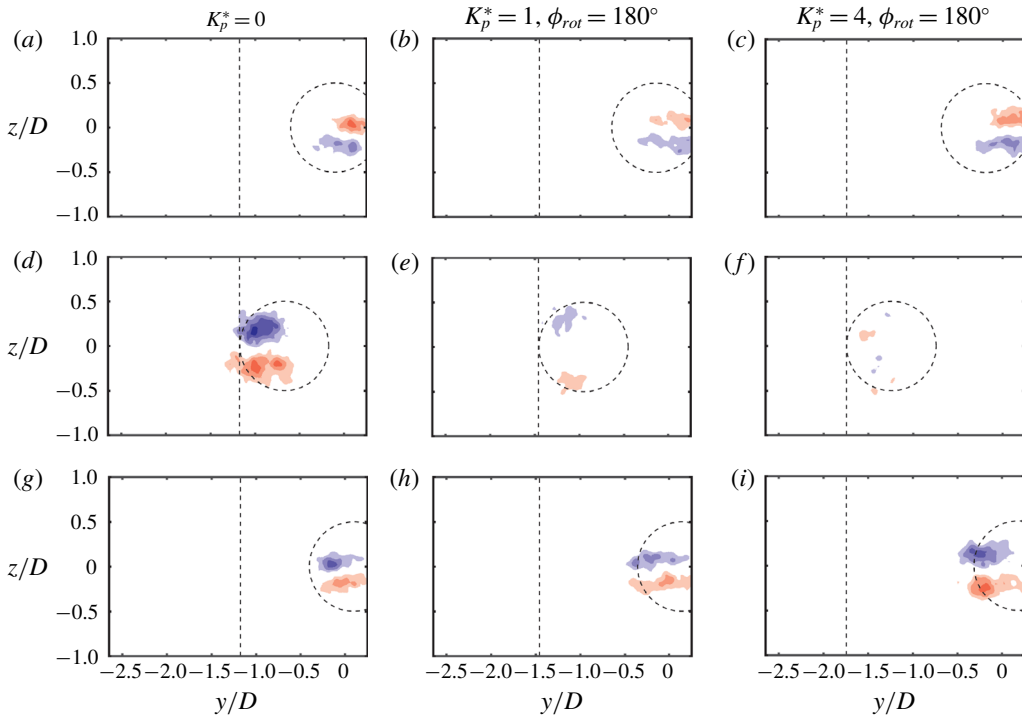
FIGURE 20. Streamwise vorticity shown in the cross-stream plane at $x/D = 1.5$ past the peak of the mode II regime ($U^* = 14$). (a,d,g) $K_p^* = 0$. (b,e,h) $K_p^* = 1$, $\phi_{rot} = 180°$. (c,f,i) $K_p^* = 4$, $\phi_{rot} = 180°$. Refer to figure 19 for further details.

of this averaging, with increased vibration, the bounds of the vortex pair stretches in the y-direction, causing the depiction of the vortex structure to morph from a circular to an elliptical shape as sphere motion increases and for the strength of the vortex structure to appear diminished.

We can observe, however, that imposed rotation with $K_p^* = 4$ and $\phi_{rot} = 180°$ results in a significant change in the timing of vortex formation, conforming with the results analysed in § 3.2, where it was reported that $\phi_{total} = 10°$. The wake structures observed for $K_p^* = 4$ and $\phi_{rot} = 180°$ resemble that presented by Govardhan & Williamson (2005) for the mode I regime where $\phi_{total} \approx 40°$.

For $K_p^* = 4$ and $\phi_{rot} = 0°$, no appreciable change to the timing of the vortex structures is evident. It can be observed, however, that the imposed rotation alters the extent of the transverse motion of the vortex structures. For the natural response, the vortex structures predominately lie inside the extremities of sphere motion depicted by the vertical black dashed lines. For $K_p^* = 4$ and $\phi_{rot} = 0°$, however, the vortex structures predominately lie outside the extremities.

Due to the large displacements observed in the mode III transition regime, and limitations of the PIV set-up, figure 20 shows the streamwise vorticity component in the transverse plane over only half the vibration cycle in the mode III transition regime ($U^* = 14$). For $K_p^* = 0$, $K_p^* = 1$ at $\phi_{rot} = 180°$, and $K_p^* = 4$ at $\phi_{rot} = 180°$, as presented in § 3.2, the total phase was found to be $170°$, $108°$ and $49°$, respectively. These changes in timing of the fluid force on the sphere are manifested in figure 20 as alterations to the timing of the streamwise vortex structures. From figure 20 it can
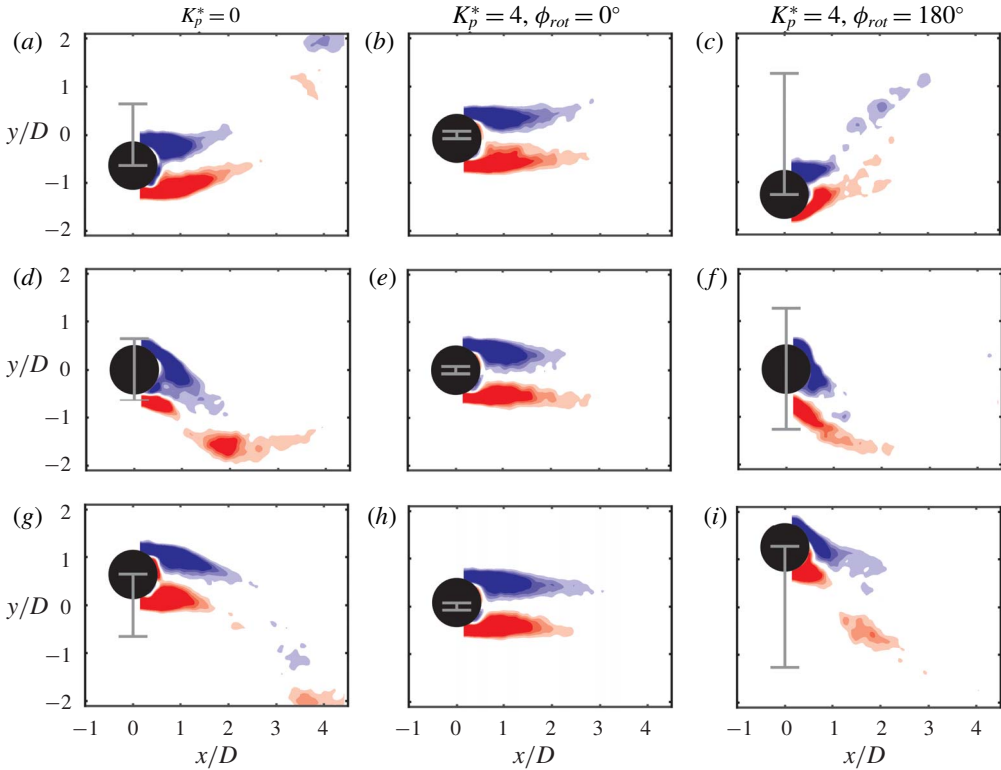
FIGURE 21. Equatorial vorticity in the mode III transition regime ($U^* = 14$). (a,d,g) $K_p^* = 0$. (b,e,h) $K_p^* = 4$, $\phi_{rot} = 0°$. (c,f,i) $K_p^* = 4$, $\phi_{rot} = 180°$. From top to bottom, each plot is separated by a quarter period. The grey line shows the extremities of sphere displacement. The black circle shows sphere location. The black line depicts the approximate centre of the wake in the x–y plane. Blue and red contours show clockwise and anti-clockwise vorticity respectively. The normalised vorticity, $\omega^* = \omega D/U$, is depicted by the colour map over eight steps in the range $\omega^* \in [-1, 1]$.

be observed that increasing the proportional gain at $\phi_{rot} = 180°$ results in increased vorticity as the sphere moves past $y/D = 0$, and decreased vorticity at the extremities of sphere displacement.

Whilst it is beneficial to examine vorticity in the y–z plane to observe the effect of rotation on the streamwise vortex structures, PIV in the equatorial plane highlights the deflection of the wake due to sphere vibration and imposed rotation. The effect of the imposed rotation is clearly visible in figure 21. It is evident that past the peak of mode II, where the rotation-induced vibration response is observed, the rotation alters the deflection of the wake. In comparison to the natural response, rotation at $\phi_{rot} = 180°$ results in a wake deflection towards the trailing side of the sphere (in the transverse sense), whilst conversely, rotation at $\phi_{rot} = 0°$ results in a deflection towards the advancing side.

4. Conclusions

A systematic investigation into the FIV response of a sphere with imposed feedback control has been conducted. Transverse rotation of the sphere in proportion to

its transverse displacement was implemented over a broad parameter space of reduced velocity, $0 \leqslant U^* \leqslant 20$, proportional gain, $0 \leqslant K_p^* \leqslant 4$, and rotation phase, $0° \leqslant \phi_{rot} \leqslant 360°$.

The imposed feedback control resulted in significant variation to the vibration response of the sphere. For rotation at $\phi_{rot} = 0°$, the vibration was found to commence at a lower reduced velocity than observed for the natural response and the subsequent maximum vibration amplitude was reduced. A similar trend to the natural response was found where total phase transitions from close to $0°$ to close to $180°$ as reduced velocity is increased, although this transition occurred progressively earlier with increasing K_p^*. A loosely inverse vibration response was seen for imposed rotation at $\phi_{rot} = 180°$, where an attenuation of vibration in the mode I regime, and subsequent significant amplification of the vibration in the mode III transition regime was found. From just prior to where the peak of the mode II regime was observed for the natural response ($U^* \approx 9$), for $K_p^* \geqslant 1$ a rotation-induced vibration regime was found. For the largest proportional gain tested, $K_p^* = 4$, at $U^* = 20$, an increase in vibration amplitude of 368 % was observed.

To determine the effect of rotation phase on the vibration response, a control law allowing rotation phase to be varied, was implemented in $15°$ increments over the range $0° \leqslant \phi_{rot} \leqslant 360°$, at three reduced velocities representative of the mode I, mode II and mode III transition regimes for the natural response. It was found that rotation phase greatly impacted the response of the sphere, and that by optimising rotation phase, vibrations could be suppressed by up to 97 %. The maximum increase in amplitude response remained that seen at $\phi_{rot} = 180°$.

PIV measurements in the wake revealed that the primary wake structures observed for the natural response, namely, two counter-rotating streamwise vortices, remained dominant across the parameter space investigated. There were, however, visible alterations to the spatial position and timing of these structures. In the rotation-induced vibration regime, significant wake deflection was observed in the equatorial plane consistent with that expected due to the Magnus effect.

As evident from our findings, there are significant benefits of closed-loop feedback control over open-loop control to either suppress or amplify the vibration response of elastically mounted three-dimensional bluff bodies. From a feedback control perspective, the control laws implemented in this study are rather simple, even if the response of the sphere was far from simple over significant portions of the parameter space. Thus, it would be of further interest to investigate the implementation of more sophisticated control laws to determine the extent to which the vibration response can be manipulated as required.

Acknowledgements

Declaration of interests

The authors report no conflict of interest.

REFERENCES

BEARMAN, P. W. 1984 Vortex shedding from oscillating bluff bodies. *Annu. Rev. Fluid Mech.* **16** (1), 195–222.

BEHARA, S., BORAZJANI, I. & SOTIROPOULOS, F. 2011 Vortex-induced vibrations of an elastically mounted sphere with three degrees of freedom at $Re = 300$: hysteresis and vortex shedding modes. *J. Fluid Mech.* **686**, 426–450.

BEHARA, S. & SOTIROPOULOS, F. 2016 Vortex-induced vibrations of an elastically mounted sphere: the effects of Reynolds number and reduced velocity. *J. Fluids Struct.* **66**, 54–68.

BERNITSAS, M., RAGHAVAN, K., BEN-SIMON, Y. & GARCIA, E. 2008 VIVACE (Vortex Induced Vibration Aquatic Clean Energy): a new concept in generation of clean and renewable energy from fluid flow. *J. Offshore Mech. Arct.* **130** (4), 041101.

BLEVINS, R. D. 1990 *Flow-Induced Vibration*, 2nd edn. Krieger Publishing Company.

DOBSON, J., OOI, A. & POON, E. K. W. 2014 The flow structures of a transversely rotating sphere at high rotation rates. *Comput. Fluids* **102**, 170–181.

ESHBAL, L., KOVALEV, D., RINSKY, V., GREENBLATT, D. & VAN HOUT, R. 2019 Tomo-PIV measurements in the wake of a tethered sphere undergoing VIV. *J. Fluids Struct.* **89**, 132–141.

ESHBAL, L., KRAKOVICH, A. & VAN HOUT, R. 2012 Time resolved measurements of vortex-induced vibrations of a positively buoyant tethered sphere in uniform water flow. *J. Fluids Struct.* **35**, 185–199.

FOURAS, A., LO JACONO, D. & HOURIGAN, K. 2008 Target-free stereo piv: a novel technique with inherent error estimation and improved accuracy. *Exp. Fluids* **44** (2), 317–329.

GIACOBELLO, M., OOI, A. & BALACHANDAR, S. 2009 Wake structure of a transversely rotating sphere at moderate Reynolds numbers. *J. Fluid Mech.* **621**, 103–130.

GOVARDHAN, R. & WILLIAMSON, C. H. K. 1997 Vortex-induced motions of a tethered sphere. *J. Wind Engng Ind. Aerodyn.* **69**, 375–385.

GOVARDHAN, R. N. & WILLIAMSON, C. H. K. 2005 Vortex-induced vibrations of a sphere. *J. Fluid Mech.* **531**, 11–47.

GRANDEMANGE, M., GOHLKE, M. & CADOT, O. 2014 Statistical axisymmetry of the turbulent sphere wake. *Exp. Fluids* **55** (11), 1838.

HÉMON, P., AMANDOLESE, X. & ANDRIANNE, T. 2017 Energy harvesting from galloping of prisms: a wind tunnel experiment. *J. Fluids Struct.* **70**, 390–402.

VAN HOUT, R., EISMA, J., ELSINGA, G. E. & WESTERWEEL, J. 2018 Experimental study of the flow in the wake of a stationary sphere immersed in a turbulent boundary layer. *Phys. Rev. Fluids* **3** (2), 024601.

VAN HOUT, R., KATZ, A. & GREENBLATT, D. 2013a Acoustic control of vortex-induced vibrations of a tethered sphere. *AIAA J.* **51** (3), 754–757.

VAN HOUT, R., KATZ, A. & GREENBLATT, D. 2013b Time-resolved particle image velocimetry measurements of vortex and shear layer dynamics in the near wake of a tethered sphere. *Phys. Fluids* **25** (7), 077102.

VAN HOUT, R., KRAKOVICH, A. & GOTTLIEB, O. 2010 Time resolved measurements of vortex-induced vibrations of a tethered sphere in uniform flow. *Phys. Fluids* **22** (8), 087101.

JAUVTIS, N., GOVARDHAN, R. & WILLIAMSON, C. H. K. 2001 Multiple modes of vortex-induced vibration of a sphere. *J. Fluids Struct.* **15** (3), 555–563.

KIM, J., CHOI, H., PARK, H. & YOO, J. Y. 2014 Inverse Magnus effect on a rotating sphere: when and why. *J. Fluid Mech.* **754**, R2.

KORKISCHKO, I. & MENEGHINI, J. R. 2012 Suppression of vortex-induced vibration using moving surface boundary-layer control. *J. Fluids Struct.* **34**, 259–270.

KRAKOVICH, A., ESHBAL, L. & VAN HOUT, R. 2013 Vortex dynamics and associated fluid forcing in the near wake of a light and heavy tethered sphere in uniform flow. *Exp. Fluids* **54** (11), 1615.

LAW, Y. Z. & JAIMAN, R. K. 2018 Passive control of vortex-induced vibration by spanwise grooves. *J. Fluids Struct.* **83**, 1–26.

MICHELIN, S. & DOARÉ, O. 2013 Energy harvesting efficiency of piezoelectric flags in axial flows. *J. Fluid Mech.* **714**, 489–504.

NAUDASCHER, E. & ROCKWELL, D. 2012 *Flow-Induced Vibrations: An Engineering Guide*. Dover Publications.

NEMES, A., ZHAO, J., LO JACONO, D. & SHERIDAN, J. 2012 The interaction between flow-induced vibration mechanisms of a square cylinder with varying angles of attack. *J. Fluid Mech.* **710**, 102–130.

PAÏDOUSSIS, M. P., PRICE, S. J. & DE LANGRE, E. 2010 *Fluid-Structure Interactions: Cross-Flow-Induced Instabilities*. Cambridge University Press.

POON, E. K. W., OOI, A. S. H., GIACOBELLO, M. & COHEN, R. C. Z. 2010 Laminar flow structures from a rotating sphere: effect of rotating axis angle. *Intl J. Heat Fluid Flow* **31** (5), 961–972.

RAJAMUNI, M. M., THOMPSON, M. C. & HOURIGAN, K. 2018a Transverse flow-induced vibrations of a sphere. *J. Fluid Mech.* **837**, 931–966.

RAJAMUNI, M. M., THOMPSON, M. C. & HOURIGAN, K. 2018b Vortex-induced vibration of a transversely rotating sphere. *J. Fluid Mech.* **847**, 786–820.

SAKAMOTO, H. & HANIU, H. 1990 A study on vortex shedding from spheres in a uniform flow. *J. Fluids Engng* **112** (4), 386–392.

SAREEN, A., ZHAO, J., LO JACONO, D., SHERIDAN, J., HOURIGAN, K. & THOMPSON, M. C. 2018a Vortex-induced vibration of a rotating sphere. *J. Fluid Mech.* **837**, 258–292.

SAREEN, A., ZHAO, J., SHERIDAN, J., HOURIGAN, K. & THOMPSON, M. C. 2018b The effect of imposed rotary oscillation on the flow-induced vibration of a sphere. *J. Fluid Mech.* **855**, 703–735.

SAREEN, A., ZHAO, J., SHERIDAN, J., HOURIGAN, K. & THOMPSON, M. C. 2018c Vortex-induced vibrations of a sphere close to a free surface. *J. Fluid Mech.* **846**, 1023–1058.

SARPKAYA, T. 2004 A critical review of the intrinsic nature of vortex-induced vibrations. *J. Fluids Struct.* **19** (4), 389–447.

SILVA-ORTEGA, M. & ASSI, G. R. S. 2017 Suppression of the vortex-induced vibration of a circular cylinder surrounded by eight rotating wake-control cylinders. *J. Fluids Struct.* **74**, 401–412.

TSUJI, Y., MORIKAWA, Y. & MIZUNO, O. 1985 Experimental measurement of the Magnus force on a rotating sphere at low Reynolds numbers. *J. Fluids Engng* **107** (4), 484–488.

VICENTE-LUDLAM, D., BARRERO-GIL, A. & VELAZQUEZ, A. 2018 Flow-induced vibration control of a circular cylinder using rotational oscillation feedback. *J. Fluid Mech.* **847**, 93–118.

WANG, C., TANG, H., YU, S. C. M. & DUAN, F. 2016 Active control of vortex-induced vibrations of a circular cylinder using windward-suction-leeward-blowing actuation. *Phys. Fluids* **28** (5), 053601.

WILLIAMSON, C. H. K. 1996 Vortex dynamics in the cylinder wake. *Annu. Rev. Fluid Mech.* **28** (1), 477–539.

WILLIAMSON, C. H. K. & GOVARDHAN, R. 1997 Dynamics and forcing of a tethered sphere in a fluid flow. *J. Fluids Struct.* **11** (3), 293–305.

WILLIAMSON, C. H. K. & GOVARDHAN, R. 2004 Vortex-induced vibrations. *Annu. Rev. Fluid Mech.* **36** (1), 413–455.

WONG, K. W. L., ZHAO, J., LO JACONO, D., THOMPSON, M. C. & SHERIDAN, J. 2017 Experimental investigation of flow-induced vibration of a rotating circular cylinder. *J. Fluid Mech.* **829**, 486–511.

WONG, K. W. L., ZHAO, J., LO JACONO, D., THOMPSON, M. C. & SHERIDAN, J. 2018 Experimental investigation of flow-induced vibration of a sinusoidally rotating circular cylinder. *J. Fluid Mech.* **848**, 430–466.

Wu, H., Sun, D. P., Lu, L., Teng, B., Tang, G. Q. & Song, J. N. 2012 Experimental investigation on the suppression of vortex-induced vibration of long flexible riser by multiple control rods. *J. Fluids Struct.* **30**, 115–132.

Zhao, J., Leontini, J., Lo Jacono, D. & Sheridan, J. 2014 Fluid-structure interaction of a square cylinder at different angles of attack. *J. Fluid Mech.* **747**, 688–721.

Zhao, J., Lo Jacono, D., Sheridan, J., Hourigan, K. & Thompson, M. C. 2018 Experimental investigation of in-line flow-induced vibration of a rotating circular cylinder. *J. Fluid Mech.* **847**, 664–699.

Zhou, T., Razali, S. F. M., Hao, Z. & Cheng, L. 2011 On the study of vortex-induced vibration of a cylinder with helical strakes. *J. Fluids Struct.* **27** (7), 903–917.